

# Measurement of the polarizations of $J/\psi$ and $\psi(2S)$ mesons promptly and non-promptly produced in pp collisions at $\sqrt{s} = 13$ TeV

Mariana Araújo and Pietro Faccioli  
LIP, Lisbon, Portugal

Carlos Lourenço  
CERN, Geneva, Switzerland

Alberto Sanchez-Hernandez  
CINVESTAV, Mexico

December 6, 2022

## Abstract

The polarizations of prompt and non-prompt  $J/\psi$  and  $\psi(2S)$  mesons are measured in pp collisions at  $\sqrt{s} = 13$  TeV, using data samples collected by CMS in 2017 and 2018, corresponding to a total integrated luminosity of  $103.3\text{ fb}^{-1}$ . The measurements, based on the analysis of the dimuon decay angular distributions, are presented as a function of the transverse momentum of the charmonium states, over a very broad range, up to more than 100 GeV.

# Contents

|          |  |           |
|----------|--|-----------|
| <b>1</b> | <b>Introduction</b>  | <b>3</b>  |
| 1.1      | Previous CMS quarkonium polarization analyses . . . . .                    | 3         |
| 1.2      | Brief overview of the analysis . . . . .                                   | 4         |
| 1.3      | Physics motivation for a high-precision polarization measurement . . . . . | 4         |
| 1.4      | Basic polarization concepts and definitions . . . . .                      | 7         |
| <b>2</b> | <b>Data and MC samples, event selection criteria, basic plots</b>          | <b>10</b> |
| 2.1      | Data samples . . . . .   | 10        |
| 2.2      | Monte-Carlo samples . . . . .  | 10        |
| 2.3      | Event selection criteria and definition of analysis samples . . . . .      | 11        |
| 2.4      | Event yields per year of data taking . . . . .                             | 15        |
| 2.5      | Illustrations of some kinematical distributions . . . . .                  | 16        |
| <b>3</b> | <b>A brief overview of the analysis</b>                                    | <b>17</b> |
| <b>4</b> | <b>Dimuon mass and lifetime dimensions</b>                                 | <b>29</b> |
| 4.1      | The dimuon mass distribution . . . . .                                     | 30        |
| 4.2      | The dimuon lifetime distribution . . . . .                                 | 35        |
| 4.3      | An interesting side remark . . . . .                                       | 39        |
| <b>5</b> | <b>Polarization measurement</b>  | <b>39</b> |
| <b>6</b> | <b>Systematic uncertainties</b>  | <b>43</b> |
| 6.1      | Potential differences between the 2017 and 2018 samples . . . . .          | 43        |
| 6.2      | Fit model of the dimuon mass distributions . . . . .                       | 44        |
| 6.3      | Single muon detection efficiencies . . . . .                               | 45        |
| 6.4      | Dimuon detection efficiencies (“ $\rho$ factor”) . . . . .                 | 46        |
| 6.5      | Potential residual azimuthal anisotropy in the helicity frame . . . . .    | 47        |
| 6.6      | Summary of the systematic uncertainties . . . . .                          | 49        |
| <b>7</b> | <b>Results</b>   | <b>49</b> |
| <b>8</b> | <b>Summary</b>   | <b>50</b> |

# 1 Introduction

This analysis note presents the measurement of the polarizations of the  $J/\psi$  and  $\psi(2S)$  mesons promptly and non-promptly produced in proton-proton collisions at  $\sqrt{s} = 13\text{ TeV}$ , on the basis of data collected in 2017 and 2018 by the CMS experiment. This is a much larger sample than the one collected in 2011, at  $7\text{ TeV}$ , which was used for the previous CMS measurement of the prompt  $J/\psi$  and  $\psi(2S)$  polarizations. Besides the obvious improvement in the statistical uncertainties, the Run 2 sample allows us to probe a much broader  $p_T$  range, extending to  $p_T$  values well in excess of those reached before.

## 1.1 Previous CMS quarkonium polarization analyses

The work described in this document represents one more step in a series of CMS measurements of the polarizations of quarkonium states. We started with the measurement of the polarizations of the Upsilon states, as a function of  $p_T$  and in two rapidity ranges, using the  $7\text{TeV}$  pp data collected by CMS in 2011 (analysis BPH-11-023) [6], a work described in detail in the analysis note AN-2012/140. This measurement implied the development of an original analysis framework, explained in the analysis note AN-2011/535 [8]. Once this first step was completed, the analysis team moved to the BPH-13-003 analysis, the measurement of the polarizations of the  $J/\psi$  and  $\psi(2S)$  states promptly produced in  $7\text{TeV}$  pp collisions [5], a work described in the analysis note AN-2013/016. This second work had the extra challenge of ensuring that the non-prompt charmonia, resulting from decays of B hadrons, could be properly removed from the signal sample, through the simultaneous analysis of the dimuon mass and pseudo-proper lifetime. The effort that went into these two analyses gave birth to two more publications: the measurement of the  $J/\psi$  and  $\psi(2S)$  cross sections in pp collisions at  $7\text{TeV}$  (BPH-14-001) [16], and the measurement of the polarizations of the Upsilon states as a function of the multiplicity of charged tracks produced in the pp collisions (HIN-15-003) [18].

The analysis BPH-13-001 represented one more step in increasing complexity: the measurement of the polarizations of the  $\chi_{c1}$  and  $\chi_{c2}$  mesons promptly produced in proton-proton collisions at  $\sqrt{s} = 8\text{TeV}$  [23]. This work is described in detail in the analysis note AN-2019/045. The difficulty of discriminating the prompt and non-prompt contributions was solved through the analysis of the dimuon pseudo-proper lifetime distribution, following an improved version of the formalism previously used in the BPH-13-003 work. The bigger challenge was the identification of an event sample of  $\chi_c$  candidates, reconstructed by combining the dimuon emitted in the  $J/\psi$  decay with a photon produced in the radiative  $\chi_c$  decay:  $\chi_c \rightarrow J/\psi\gamma$ . The photon was exclusively detected using conversions to  $e^+e^-$  pairs, reconstructed in the CMS silicon tracker, which provides a  $\chi_c$  mass measurement with sufficient resolution to discriminate the  $\chi_{c1}$  and  $\chi_{c2}$  components. This is a crucial aspect of the analysis, in view of reaching an independent measurement of the polarizations of the two mesons. The technique used for the detection of photon conversions had been previously de-

veloped in CMS and was at the basis of two CMS publications, reporting the cross-section ratios of P-wave states:  $\chi_{c2}/\chi_{c1}$  (BPH-11-010) [4] and  $\chi_{b2}/\chi_{b1}$  (BPH-13-005) [17].

Along the way, four PhD theses have been prepared and defended, by Valentin Knünz [19], Ilse Krätschmer [20], Chris Ferraioli [15], and Thomas Madlener [21], which constitute an exceptional source of detailed and pedagogical information, well suited for the “interested readers”.

## 1.2 Brief overview of the analysis

The analysis provides the polarizations of the *prompt* and *non-prompt*  $J/\psi$  and  $\psi(2S)$  mesons. The prompt and non-prompt events are selected using the pseudo-proper lifetime observable. Besides the directly produced component, the prompt  $J/\psi$  event sample includes “feed-down decays” of heavier charmonium states: around 8% of mesons produced in  $\psi(2S)$  decays and around 25% produced in  $\chi_c$  decays [13]. No such feed-down sources contribute to the  $\psi(2S)$  sample. The non-prompt mesons are produced in (inclusive) decays of B mesons.

The measurement is, as in all the previous analyses, based on the analysis of the angular distributions of the dimuons resulting from the decay of the quarkonium mesons. The polarization extraction method used in this analysis uses the information content of the dimuon mass distribution to separate the  $J/\psi$  signal contribution from the muon pairs resulting from other processes (mostly pairs of muons resulting from decays of uncorrelated heavy flavour mesons). The 4-momentum vectors of the two muons, containing the spin alignment information of the decaying meson, are used to extract the anisotropy parameters  $\lambda$  (see next section) in each independent  $p_T$  bin. Given that, as expected, no rapidity-dependences have been seen in the previous measurements, this analysis is made integrated over the dimuon rapidity window  $|y| < 1.2$ , without splitting this (relatively narrow) mid-rapidity window into thinner bins.

The physics result is reported in the form of the polar anisotropy parameter in the centre-of-mass helicity frame,  $\lambda_\theta^{\text{HX}}$ . The azimuthal anisotropy is also studied, essentially to confirm that, in the HX frame, it can be neglected. Residual azimuthal anisotropies are taken into account as a systematic uncertainty in  $\lambda_\theta^{\text{HX}}$ .

## 1.3 Physics motivation for a high-precision polarization measurement

Vector particles (Z, W, Drell–Yan) are generally produced with maximal polarization. Even if for a given  $p_T$ , in a given frame, the polarization can be zero, there must always exist a kinematical domain and an “optimal” frame where it approaches maximal values. In fact, vector states are intrinsically polarized.

This statement can be presented in the form of a theorem (see Ref. [12] for details): for any subprocess producing a  $J = 1$  state  $|V; J, J_z\rangle = a_{-1}|1, -1\rangle + a_0|1, 0\rangle + a_{+1}|1, +1\rangle$ , there exists a quantization axis with respect to which the  $J_z = 0$  component vanishes, which implies that  $\lambda_\theta = +1$  along that axis. This is

intuitively consistent with the classical expectation: a vector of modulus unity has always projection  $\pm 1$  along *some* axis.

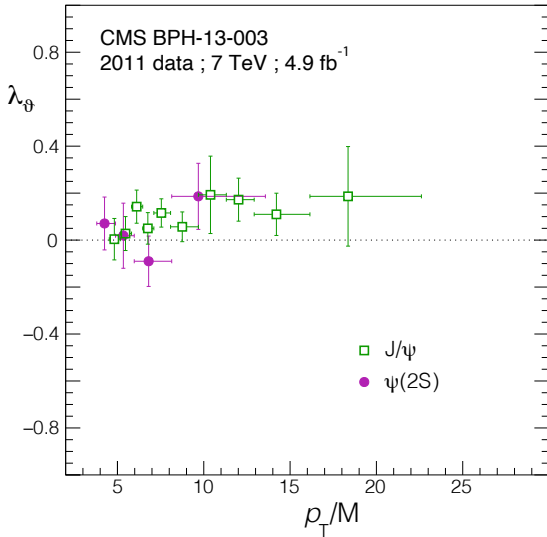


Figure 1: Polar anisotropy parameter,  $\lambda_\theta$ , as a function of the quarkonium mass-scaled  $p_T$ , for the  $J/\psi$  and  $\psi(2S)$  promptly-produced in the 7TeV pp collisions collected by CMS in 2011.

Given this understanding, it is surprising to see that the BPH-13-003 results indicate that the  $J/\psi$  and  $\psi(2S)$  polarizations are close to zero, as illustrated in Fig. 1. The only reasonable explanations are that we measure negligible polarizations because 1) we are seeing the superposition of several production subprocesses that, thanks to a “fortunate coincidence”, cancel each other, or 2) we are seeing the result of a “randomization step” that completely smears away the initial strong polarization, so that we end up with almost isotropic dimuon angular decay distributions.

This experimental observation does not match what one would naturally expect in the context of the NRQCD theoretical approach. Indeed, within NRQCD, the  $J/\psi$  and  $\psi(2S)$  production should be dominated by three colour octet terms (the colour singlet having a negligible contribution) of similar magnitude: the  $^1S_0^{[8]}$ ,  $^3S_1^{[8]}$ , and  $^3P_J^{[8]}$  (pre-resonant) c $\bar{c}$ states. As shown in Fig. 2, these three terms have rather different polarizations. The  $^1S_0^{[8]}$  term leads to mesons that are intrinsically polarized along the *unobservable*  $^1S_0^{[8]}$ -state direction, so that they look unpolarized, because of rotational smearing. Instead, the  $^3S_1^{[8]}$  and  $^3P_J^{[8]}$  octets produce strongly polarized quarkonia states, with the  $\lambda_\theta$  of the  $^3S_1^{[8]}$  contribution being close to the maximum physical limit, +1, and that of the  $^3P_J^{[8]}$  term being even larger than that limit. With suitable relative weights, one can add the three terms so that the sum gives zero at a given  $p_T$ .

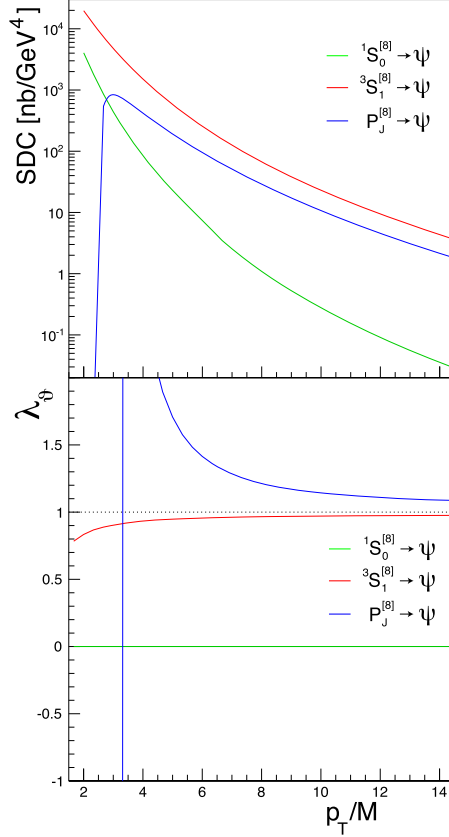


Figure 2: Differential cross sections (“SDCs”, top) and polarizations ( $\lambda_\theta$ , bottom) of the three colour octets expected to dominate  $J/\psi$  and  $\psi(2S)$  production in the NRQCD framework, computed at NLO.

value but, as we can easily see by looking at the three very different curves shown on the bottom panel of Fig. 2, it is not possible to reach a null sum over a broad  $p_T$  range, a conclusion that is in contradiction with the seemingly flat measured patterns seen in Fig. 1.

However, the relatively poor precision of the measurements shown in Fig. 1 leave the door open to the possibility of non-flat trends, so that, for now, we can consider the following three scenarios:

- 1) we are seeing an *accidental* cancellation of the  ${}^3S_1^{[8]}$  and  ${}^3P_J^{[8]}$  terms in a narrow  $p_T$  domain, in which case a more precise measurement will reveal a non-flat trend;
- 2) we are in the presence of an exact degeneracy between the colour-octet terms, at least as computed at NLO, so that their sum is identical to the

(unpolarized)  ${}^1S_0^{[8]}$  term alone, in which case we would have to conclude that the NRQCD expansion is not a natural description of nature;

- 3) we are seeing that the  ${}^1S_0^{[8]}$  term completely dominates over the other two, in which case we would have clear evidence showing that the NRQCD  $v^2$  scaling hierarchy fails for charmonium production.

The prompt  $J/\psi$  polarization measurement made using the 2017 and 2018 data samples, reported in this AN, is sufficiently precise to see if the trend of  $\lambda_\theta$  with  $p_T$  is essentially flat or starts showing a significant slope at some  $p_T$  value. So, the main goal of this measurement is to evaluate if the pattern of  $\lambda_\theta$  as a function of  $p_T$  can be well described by a constant or if we have significant evidence of a departure from a flat trend, above some  $p_T$  value. The measurement of the prompt  $\psi(2S)$  polarization, although less precise than that of the  $J/\psi$ , given the smaller event samples, offers interesting complementary information because it is not affected by effects caused by the feed-down decays of the  $\chi_c$  mesons. That result is not expected to be sufficiently precise to help determining the shape of the  $p_T$  dependence of  $\lambda_\theta$  but will address another equally interesting question: is  $\lambda_\theta$  different from zero for the *directly produced* vector quarkonia? Furthermore, the *difference* between the  $\psi(2S)$  and  $J/\psi$  polarizations can provide precise information about the polarizations of the  $\chi_{c1}$  and  $\chi_{c2}$  states, as explained in Ref. [10].

This AN also reports the measurement of the polarizations of non-prompt  $J/\psi$  and  $\psi(2S)$  mesons, produced in decays of unreconstructed B mesons and detected in the dimuon channel, using the same 2017 and 2018 data samples. More than simply a byproduct, non-prompt  $J/\psi$  polarization measurements can provide interesting information on quarkonium hadroproduction, complementing the studies of prompt production. This is a measurement that can be directly compared to predictions reported in Ref. [9].

## 1.4 Basic polarization concepts and definitions

The average polarization of any  $J^{PC} = 1^{--}$  quarkonium can be determined by measuring its dilepton decay distribution, which has the general observable form [12, 11]

$$W(\cos \vartheta, \varphi | \vec{\lambda}) = \frac{3/(4\pi)}{(3 + \lambda_\theta)} (1 + \lambda_\theta \cos^2 \vartheta + \lambda_\varphi \sin^2 \vartheta \cos 2\varphi + \lambda_{\theta\varphi} \sin 2\vartheta \cos \varphi), \quad (1)$$

where  $\vartheta$  and  $\varphi$  are the polar and azimuthal angles of the positive lepton in the quarkonium rest frame with respect to, respectively, a suitably defined polarization axis  $z$  and the plane containing the momenta of the colliding beams and of the quarkonium (the *production plane*,  $xz$ ), as illustrated in Fig. 3. The shape of the decay angular distribution is defined by the polarization parameters  $\lambda_\theta$ ,  $\lambda_\varphi$ , and  $\lambda_{\theta\varphi}$ .

Given that we are studying mid-rapidity and high- $p_T$  quarkonia, it is very reasonable to focus the analysis by presenting the main results in the form of

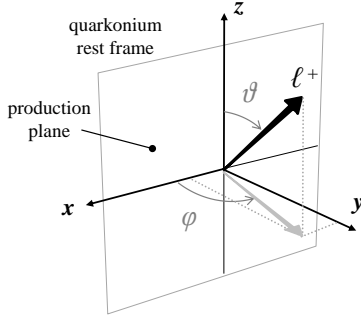


Figure 3: Coordinate system for the measurement of a dilepton decay angular distribution in the quarkonium rest frame. The  $y$  axis is perpendicular to the plane containing the momenta of the colliding beams. The choice of the definition of the polarization axis  $z$  determines the measurement frame. From Ref. [14].

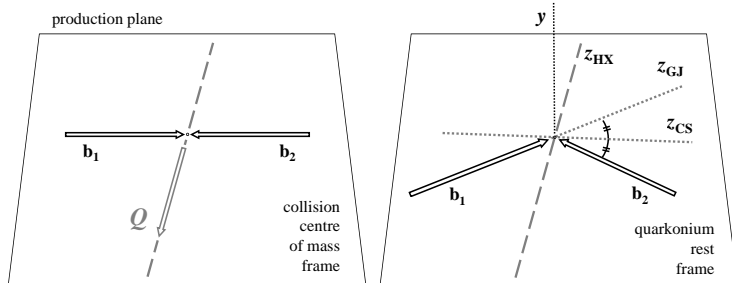


Figure 4: Schematic illustration of reference frames frequently used in studies of quarkonium production. In this study, the polarization axis  $z$  is chosen according to the HX convention. From Ref. [14].

the polar anisotropy parameter,  $\lambda_\theta$ , in the centre-of-mass helicity (HX) frame, where the  $z$  axis coincides with the flight direction of the meson in the centre-of-mass frame of the colliding hadrons, as illustrated in Fig. 4. Other anisotropy parameters offer useful crosschecks.

The polar anisotropy parameter is determined using a simplified version of Eq. 1, integrating over the azimuthal decay angle,

$$W(\cos \theta) \propto 1 + \lambda_\theta \cos^2 \vartheta . \quad (2)$$

Translating this equation into words, we project the “final analysis ntuple” into the  $\cos \theta$  variable, only selecting dimuons in the prompt region and in the  $J/\psi$  “signal mass window”, and then fit that distribution with a parabolic function to determine  $\lambda_\theta$ .

In reality, things are more complex than suggested by this simple description. To start with, the analysis is made using the observable  $|\cos \theta|$ , so as to

decrease the statistical uncertainties shown in the figures. Indeed, the symmetry of the underlying physics implies that the distribution must be symmetric around zero and, hence, there is no information gain in using the  $\cos \theta$  variable. More importantly, the analysis is made in many  $p_T$  bins, in order to measure the  $p_T$  dependence of  $\lambda_\theta$ . The  $p_T$  bins are relatively narrow, especially at low  $p_T$ , not so much because we need to have a high granularity to determine a potential trend of  $\lambda_\theta$  with  $p_T$  but rather to ensure that, within those bins, the variation of the polarization (if there is any) can be neglected. It might be worth noting that the integration over the  $|y| < 1.2$  range is justified by the observation that no variations of the polarization are expected in any theory model within that relatively narrow mid-rapidity range, a prediction in good agreement with the results of the BPH-13-003 analysis, which were provided in two rapidity ranges for the  $J/\psi$  meson,  $|y| < 0.6$  and  $0.6 < |y| < 1.2$ . In these conditions, we can write Eq. 2 as

$$W(|\cos \theta|, p_T) \propto 1 + \lambda_\theta(p_T) \cos^2 \vartheta . \quad (3)$$

A bigger challenge of the analysis is that we cannot use Eq. 3 to directly fit the measured (“raw data”)  $\cos \theta$  distributions because they are affected by sculpting effects introduced by the limited acceptance coverage of the detector and by the efficiencies of the trigger and reconstruction steps. In other words, the fit must be done on distributions previously corrected for those experimental effects. As in all other previous analyses, we evaluate the detection acceptance through a very detailed (“full”) simulation of the whole detection chain, from the trigger step to the offline reconstruction and event selection criteria. The Monte Carlo simulation is made assuming unpolarized production (i.e., a flat  $\cos \theta$  distribution), so that any non-flat trends we see in the simulated distributions are caused by the convolution of all the detection effects (mostly the acceptance, but also the single muon and dimuon efficiencies). So, we start by dividing (in each  $p_T$  bin) the measured  $|\cos \theta|$  distribution by the simulated one, before we perform the fit using Eq. 3. In this way, the only remaining reason for potential modulations of the angular distribution is the polarization of the measured charmonium samples.

To probe the possible existence of a residual azimuthal anisotropy, the analysis has been redone, in exactly the same way (same  $p_T$  bins, etc.) replacing the  $|\cos \theta|$  polar angle by the  $\varphi$  azimuthal angle. The  $\varphi$  distributions, corrected for acceptance as previously explained, are fitted with the function

$$W(\varphi|\vec{\lambda}) \propto 1 + \beta \cos 2\varphi , \quad (4)$$

with  $\beta = (2 \lambda_\varphi)/(3 + \lambda_\theta)$ , obtained from Eq. 1 integrating over the polar decay angle.

## 2 Data and MC samples, event selection criteria, basic plots

### 2.1 Data samples

The analysis uses the data samples collected by CMS during the 2017 and 2018 running periods. The events were collected with two dimuon triggers, for the  $J/\psi$  and the  $\psi(2S)$  cases, the HLT paths being called `HLT_Dimuon25_Jpsi` and `HLT_Dimuon18_PsiPrime`, respectively. The trigger requires an opposite-sign muon pair invariant mass, in the ranges 2.9–3.33GeV for the  $J/\psi$  and 3.35–4.05GeV for the  $\psi(2S)$ , with a distance of closest approach between the two muons smaller than 0.5cm and a fit of the positions and momenta of the two muon candidates to a common vertex (“dimuon vertex fit”)  $\chi^2$  probability larger than 0.5%. In addition, the dimuon transverse momentum must be larger than 24.9GeV, for the  $J/\psi$ , or 17.9GeV, for the  $\psi(2S)$ . No explicit  $p_T$  requirement was imposed on the single muons at trigger level. The dimuon rapidity is restricted to  $|y| < 1.25$  because this is the most interesting kinematical region for the physics analyses and also where the measurements have the best resolutions. Including forward rapidity dimuons (the full CMS rapidity coverage in Run 2 is  $|y| < 2.5$ ) would have implied increasing the  $p_T$  threshold to larger values, to keep the total trigger rate within the allocated trigger bandwidth.

The integrated luminosity adds up to  $103.3\text{fb}^{-1}$ , distributed as 42.0 and  $61.3\text{fb}^{-1}$  for 2017 and 2018, respectively. These values are computed with the standard `brilcalc` tool [1] and take into consideration that we only use data collected in the certified lumisections, as listed in the following JSON files, one per year of data taking:

- `Cert_294927-306462_13TeV_UL2017_Collisions17_MuonJSON`
- `Cert_314472-325175_13TeV_Legacy2018_Collisions18_JSON_MuonPhys`

It should be kept in mind that the polarization measurement is completely independent of the exact value of the integrated luminosity, which is only reported to offer a qualitative measure of the size of the analysed event sample.

The ntuples were produced with the so-called “UltraLegacy production”, the latest available reconstruction software. Table 1 lists all the (MiniAOD) samples and respective run ranges.

The reconstructed data were processed ensuring that both reconstructed muons must match, in pseudorapidity and azimuthal angle, those that triggered the detector readout. Both muon tracks must have more than five hits in the tracker, at least one of them being in a pixel detector layer. They must also fulfill the other standard quarkonium muon selection cuts (the so-called “soft-muon selection” [22]).

### 2.2 Monte-Carlo samples

The analysis also uses simulated (MC) event samples, generated with the PYTHIA 8 event generator [24], with the standard charmonium production settings. The

Table 1: Data samples and run ranges used in the current analysis.

| Data sample                      | Run range     |
|----------------------------------|---------------|
| Run2017B-09Aug2019_UL2017-v1     | 297047–299329 |
| Run2017C-09Aug2019_UL2017-v1     | 299368–302029 |
| Run2017D-09Aug2019_UL2017-v1     | 302031–302491 |
| Run2017E-09Aug2019_UL2017-v1     | 303824–304671 |
| Run2017F-09Aug2019_UL2017-v1     | 305040–305364 |
| Run2018A-12Nov2019_UL2018_rsb-v1 | 315257–316995 |
| Run2018B-12Nov2019_UL2018-v1     | 317080–319310 |
| Run2018C-12Nov2019_UL2018-v1     | 319337–320008 |
| Run2018D-12Nov2019_UL2018-v1     | 320500–321068 |

MC samples are exclusively composed of prompt mesons (pure signal). The generated  $J/\psi$  and  $\psi(2S)$  mesons only decay to dimuons, to avoid wasting CPU. The decays are isotropic, i.e. reflecting unpolarized production. Final state QED radiation is generated for the muons through the **PHOTOS** 3.61 package [7]. The simulated events include multiple pp interactions in the same or nearby beam crossings (pileup), with a distribution matching the one observed in data (the average number of pileup interactions was 32 in the 2017–2018 period). The simulated events are then processed through a detailed simulation of the CMS detector, based on the **GEANT4** package [2], using the same trigger and reconstruction algorithms as used to collect and process the data. These samples are independently generated for each of the two years and are expected to faithfully reproduce the running conditions of the CMS experiment during the data collection periods. All samples are generated with the single muons in the kinematical window  $p_T > 4\text{GeV}$  and  $|\eta| < 1.5$ .

Some of the MC samples were “officially produced”. They were complemented by additional MC samples, generated “privately” following the procedures used in the official production, so that the final results are not significantly affected by the statistical uncertainties of the simulated samples.

To improve the statistical uncertainties at high  $p_T$ , several complementary  $J/\psi$  MC samples were generated. They are used in four exclusive ranges: 25–45; 45–50; 50–70; 70–120GeV. For the  $\psi(2S)$  case, a single high-statistics MC sample was produced.

### 2.3 Event selection criteria and definition of analysis samples

For easy reference, we list in this section the offline event selection criteria used to define the “final-analysis event sample”:

- Single muon kinematical cuts:  $p_T > 5.6\text{GeV}$  and  $|\eta| < 1.4$ ;
- Dimuon rapidity cuts:  $|y| < 1.2$ ;
- Dimuon  $p_T$  cuts:  $25 < p_T < 120\text{GeV}$  ( $J/\psi$ ) or  $20 < p_T < 100\text{GeV}$  ( $\psi(2S)$ );

- Dimuon mass:  $2.92 < m < 3.28 \text{ GeV}$  ( $J/\psi$ ) or  $3.4 < m < 4.0 \text{ GeV}$  ( $\psi(2S)$ );
- Dimuon vertex fit  $\chi^2$  probability larger than 1%.

The observables used in all of these event selection steps are computed with the standard Onia2MuMu package, which has been used in analogous ways in all the CMS quarkonium analyses made on the basis of the Run 1 data, as well as in the paper reporting quarkonium production cross sections with the 2015 data (BPH-15-005). The source code, continuously updated within the BPH PAG throughout the last 10 years, can be consulted in Ref. [3].

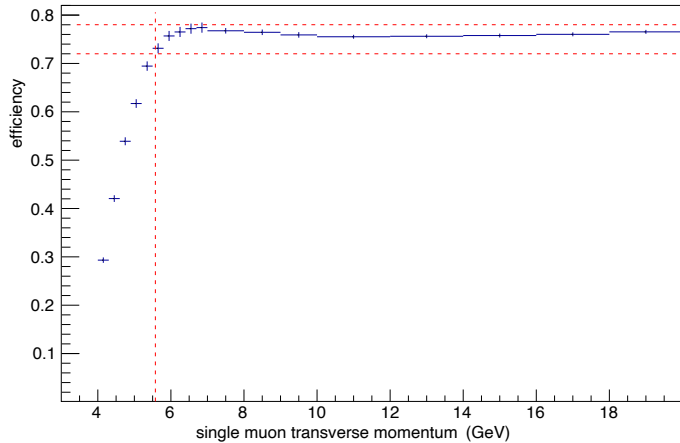


Figure 5: Single muon efficiency as a function of  $p_T$ , as evaluated from the simulated events.

The single muon  $p_T$  cut is set at 5.6 GeV so that all the selected muons have detection efficiencies that vary by less than 5%. as can be seen in Fig. 5. In other words, all the analysed events have both muons in the “plateau” region of the detection efficiency. It is important to keep in mind that the polarization measurement is insensitive to the absolute magnitude of the detection efficiencies, so that we only need to worry about the variations of efficiency within the analysed sample matter. By avoiding the  $p_T$  dependent “turn-on” region of the efficiency curve, we minimise the potential residual effects of a less-than-perfect efficiency correction, so that the results become almost unaffected by the uncertainties on the assumed efficiencies.

The  $J/\psi$  polarization parameter  $\lambda_\varrho$  is measured, in the helicity frame and as a function of  $p_T$ , using the  $|\cos\theta|$  distributions measured in six independent event samples, defined by two ranges in the dimuon lifetime (prompt and non-prompt) and three in the dimuon mass ( $J/\psi$  region, left and right sidebands):

- PR:  $|c\tau| < 50 \mu\text{m}$ ; NP:  $100 < c\tau < 500 \mu\text{m}$ ;
- $J/\psi$  mass region: 3.0–3.2 GeV; LSB: 2.92–2.95 GeV; RSB: 3.21–3.28 GeV.

The  $\psi(2S)$  analysis is done in a completely analogous way, simply replacing the  $J/\psi$  mass regions by the corresponding  $\psi(2S)$  regions:

- PR:  $|c\tau| < 50 \mu\text{m}$ ; NP:  $100 < c\tau < 500 \mu\text{m}$ ;
- $\psi(2S)$  mass region: 3.57–3.81 GeV; LSB: 3.4–3.52 GeV; RSB: 3.82–4.0 GeV.

The NP and 3.0–3.2 GeV 2D region includes the non-prompt  $J/\psi$  mesons (from B decays) plus a background contribution from non-prompt “mass continuum” muon pairs. The PR and 3.0–3.2 GeV 2D region (which we label as “Peak”) contains the prompt  $J/\psi$  mesons plus background contributions from prompt “mass continuum” muon pairs and “non-prompt”  $J/\psi$  mesons.

The MC samples are exclusively composed of prompt  $J/\psi$  mesons.

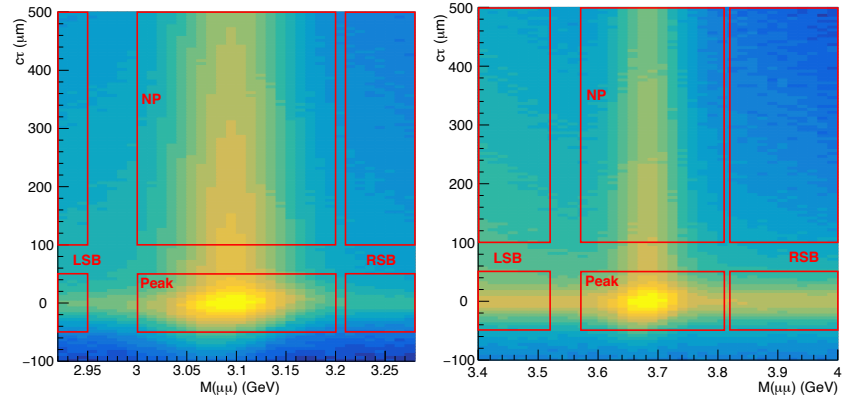


Figure 6: Two-dimensional event distribution in the dimuon lifetime vs. mass dimensions, for the 2018  $J/\psi$  (left) and  $\psi(2S)$  (right) data samples, showing the rectangular windows defining the six regions used in the analysis. The Peak windows include the prompt signal as well as the two background contaminations. The five “control windows” are used to evaluate the  $|\cos \theta|$ distributions of those backgrounds.

For illustration purposes, the six windows used in the  $J/\psi$  and  $\psi(2S)$  analysis are graphically represented in Fig. 6. The dimuon mass resolution at the  $J/\psi$  mass is around 20–40 MeV, depending on dimuon rapidity and  $p_T$ , so that the range  $3.0 < m < 3.2 \text{ GeV}$  corresponds to a coverage of around  $\pm 3 \sigma$ . The dimuon pseudo-proper lifetime observable,  $c\tau$ , is the distance between the dimuon vertex and the primary vertex. It is measured with a resolution of around 20–30  $\mu\text{m}$ , so that the range  $|c\tau| < 50 \mu\text{m}$  corresponds to a coverage of around  $2 \sigma$ . The primary vertex is selected among all the reconstructed proton-proton collision vertices in the event as the one closest to the line extrapolating the dimuon momentum back to the beam line.

The  $J/\psi$  polarization is measured in 19  $p_T$  bins, of widths increasing with increasing  $p_T$ :

- 10 bins of 2.5 GeV in the range 25–50 GeV;
- 6 bins of 5 GeV in the range 50–80 GeV;
- 2 bins of 10 GeV in the range 80–100 GeV;
- 1 bin of 20 GeV in the range 100–120 GeV.

Given the smaller event sample, the  $\psi(2S)$  polarization measurement is made in only 8  $p_T$  bins, of variable width:

- 4 bins of 5 GeV in the range 20–40 GeV;
- 3 bins of 10 GeV in the range 40–70 GeV;
- 1 bin of 30 GeV in the range 70–100 GeV.

In each of those  $p_T$  bins, the  $|\cos \theta|$ -distribution (or ratio of distributions) is analysed in 20 equidistant bins between 0 and 1.

## 2.4 Event yields per year of data taking

After applying the event selection criteria described in the previous section, we are left with almost 15 million prompt and almost 11 million non-prompt  $J/\psi$  dimuons with  $p_T$  between 25 and 120 GeV. The number of  $\psi(2S)$  events is significantly smaller: 2.1 million prompt and 1.3 million non-prompt. All the event yields are collected in Tables 2 and 3.

Table 2: Event yields of the measured and simulated  $J/\psi$  samples, for the 2017 and 2018 sets, per  $p_T$  range (in GeV).

| 2017 |                                 | [25, 45] | [45, 50] | [50, 70] | [70, 120] | [25, 120] |
|------|---------------------------------|----------|----------|----------|-----------|-----------|
| Data | Prompt signal region (Peak)     | 5.380 M  | 0.209 M  | 0.282 M  | 0.073 M   | 5.944 M   |
|      | Non-prompt region (NP)          | 3.883 M  | 0.180 M  | 0.253 M  | 0.068 M   | 4.384 M   |
|      | Prompt left mass SB (PRLSB)     | 44.6 k   | 2.1 k    | 3.0 k    | 1.0 k     | 50.7 k    |
|      | Prompt right mass SB (PRRSB)    | 52.9 k   | 2.9 k    | 4.5 k    | 1.6 k     | 61.9 k    |
|      | Non-prompt left mass SB (NPLSB) | 62.1 k   | 2.9 k    | 4.0 k    | 1.0 k     | 70.1 k    |
|      | Non-prompt right mass SB (NPRS) | 66.9 k   | 3.2 k    | 4.5 k    | 1.2 k     | 75.9 k    |
| MC   | only Peak region                | 20.508 M | 1.555 M  | 1.999 M  | 1.275 M   | 25.337 M  |
| 2018 |                                 | [25, 45] | [45, 50] | [50, 70] | [70, 120] | [25, 120] |
| Data | Prompt signal region (Peak)     | 7.982 M  | 0.307 M  | 0.416 M  | 0.107 M   | 8.813 M   |
|      | Non-prompt region (NP)          | 5.746 M  | 0.265 M  | 0.373 M  | 0.100 M   | 6.484 M   |
|      | Prompt left mass SB (PRLSB)     | 69.2 k   | 3.2 k    | 4.7 k    | 1.4 k     | 78.5 k    |
|      | Prompt right mass SB (PRRSB)    | 79.5 k   | 4.4 k    | 6.8 k    | 2.4 k     | 93.1 k    |
|      | Non-prompt left mass SB (NPLSB) | 97.1 k   | 4.4 k    | 6.2 k    | 1.7 k     | 109.4 k   |
|      | Non-prompt right mass SB (NPRS) | 101.2 k  | 4.8 k    | 6.5 k    | 1.8 k     | 114.2 k   |
| MC   | only Peak region                | 20.984 M | 1.590 M  | 1.760 M  | 1.599 M   | 25.933 M  |

Table 3: Event yields of the measured and simulated  $\psi(2S)$  samples, for the 2017 and 2018 sets, in the full  $p_T$  range.

|      |                                 | 2017    | [20, 100] |
|------|---------------------------------|---------|-----------|
| Data | Prompt signal region (Peak)     | 0.854 M |           |
|      | Non-prompt region (NP)          | 0.543 M |           |
|      | Prompt left mass SB (PRLSB)     | 162.0 k |           |
|      | Prompt right mass SB (PRRSB)    | 183.9 k |           |
|      | on-prompt left mass SB (NPLSB)  | 147.1 k |           |
|      | Non-prompt right mass SB (NPRS) | 56.7 k  |           |
| MC   | only Peak region                | 5.572 M |           |
|      |                                 | 2018    | [20, 100] |
| Data | Prompt signal region (Peak)     | 1.276 M |           |
|      | Non-prompt region (NP)          | 0.808 M |           |
|      | Prompt left mass SB (PRLSB)     | 242.9 k |           |
|      | Prompt right mass SB (PRRSB)    | 275.6 k |           |
|      | on-prompt left mass SB (NPLSB)  | 220.6 k |           |
|      | Non-prompt right mass SB (NPRS) | 84.9 k  |           |
| MC   | only Peak region                | 6.660 M |           |

## 2.5 Illustrations of some kinematical distributions

The next figures illustrate the dimuon mass,  $p_T$ , rapidity, and lifetime distributions, and how the measured and simulated spectra compare to each other. These illustrations are made with the 2018  $J/\psi$  data.

Figure 7-left compares the measured and simulated invariant mass distributions of the prompt dimuons ( $|c\tau| < 50 \mu\text{m}$ ) in the 25–45GeV (red) and 70–120GeV (blue)  $p_T$  ranges. There are no continuum background dimuons in the MC samples, which are pure (prompt) signal. We see that the mass resolution degrades from low to high  $p_T$ . Figure 7-right shows the  $p_T$  distributions of the measured Peak data (black) and of the samples simulated in four  $p_T$  ranges: 25–46GeV (“low  $p_T$  range”, in red), 40–52GeV (“mid  $p_T$  range”, in purple),  $> 46\text{GeV}$  (“high  $p_T$  range”, in green), and  $> 66\text{GeV}$  (“highest  $p_T$  range”, in blue). It should be kept in mind that the “data” sample includes contaminations from  $J/\psi$  dimuons produced in  $B$  meson decays (even if with  $|c\tau| < 50 \mu\text{m}$ ) and from “continuum mass dimuons”, while the simulated samples are pure prompt  $J/\psi$  signal. We have verified that the dimuon kinematic distributions obtained in the different MC samples are compatible with each other in their common  $p_T$  ranges.

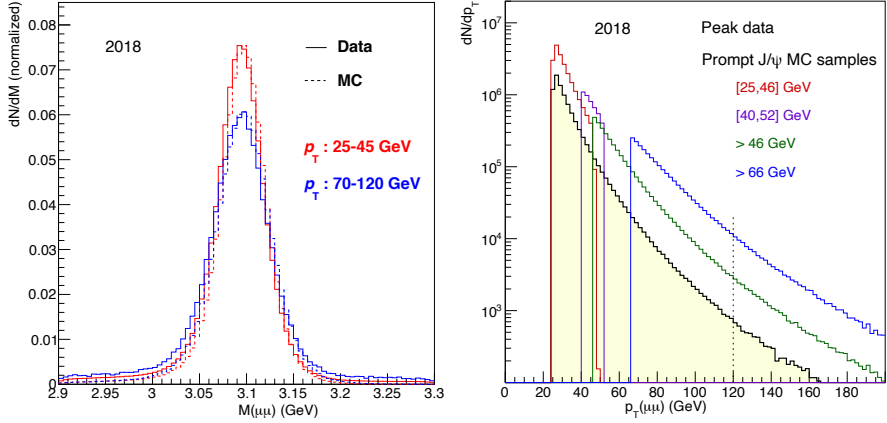


Figure 7: Left: Invariant mass distribution of the measured (solid histograms) and simulated (dashed histograms) prompt dimuons ( $|c\tau| < 50 \mu\text{m}$ ), in the 25–45GeV (red) and 70–120GeV (blue)  $p_T$  ranges. Right: Measured (black histogram)  $p_T$  distribution of the dimuons in the prompt  $\text{J}/\psi$  signal region (Peak window:  $|c\tau| < 50 \mu\text{m}$  and  $3.0 < m < 3.2 \text{GeV}$ ), compared to the distributions of the four samples of simulated events (red, purple, green, and blue histograms).

Figure 8 compares the data and MC rapidity distributions, in the four  $p_T$  ranges. The right panel provides an easier comparison of the shapes, by scaling the MC distributions. The data-MC agreement is quite remarkable.

As previously mentioned and graphically shown in Fig. 6, the Peak, PR LSB, and PR RSB event samples only include dimuons of pseudo-proper lifetime between  $-50$  and  $+50 \mu\text{m}$ . Instead, the NP event sample is composed of dimuons with pseudo-proper lifetime between  $100$  and  $500 \mu\text{m}$  (and only in the mass window  $3 < m < 3.2 \text{GeV}$ ). Figure 9 shows the lifetime distribution of the measured  $\text{J}/\psi$  dimuons, indicating the prompt and non-prompt windows with the vertical dashed lines and the two horizontal arrows. No simulated distributions are shown here because the MC is exclusively composed of prompt signal  $\text{J}/\psi$  events. We can see that the resolution of the lifetime measurement improves from low to high  $p_T$  and that the NP fraction increases with  $p_T$  and then flattens out.

The next figures provide equivalent illustrations for the  $\psi(2S)$  case.

### 3 A brief overview of the analysis

As previously mentioned, the polarization measurement is made by fitting Eq. 2 to the measured  $|\cos \theta|$  distribution, after correcting it for acceptance and efficiency effects, which is done by dividing it by the corresponding MC distribution. Given that the analysis is made as a function of  $p_T$ , we can say that the basic inputs for the polarization measurement are the two-dimensional  $|\cos \theta|$  vs.  $p_T$

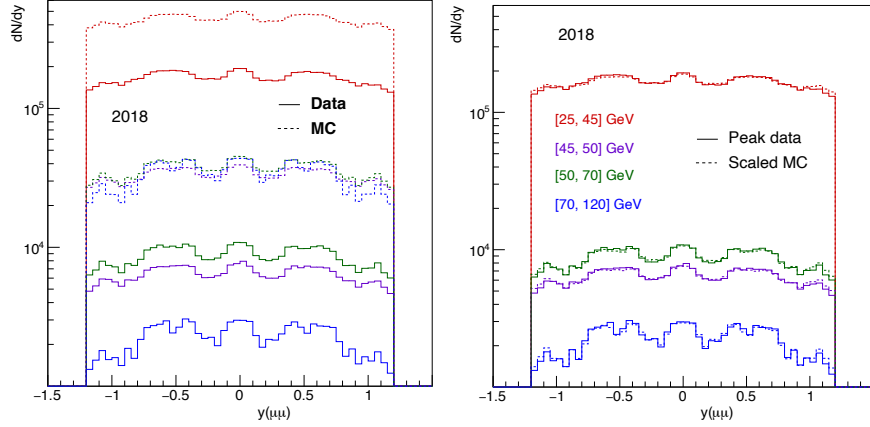


Figure 8: Rapidity distributions of the measured (solid histograms) and simulated (dashed histograms) prompt dimuons in the  $J/\psi$  mass region (Peak), in four  $p_T$  ranges (red, purple, green, and blue histograms), before (left) and after (right) rescaling the MC distributions for an easier comparison with the data shapes.

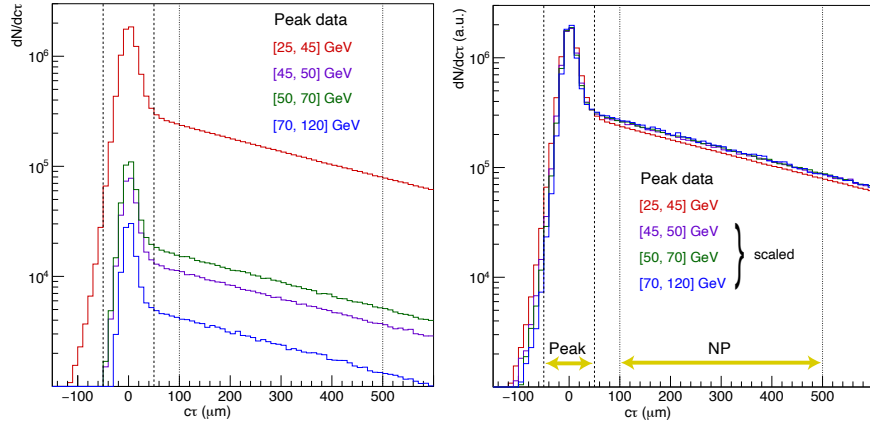


Figure 9: Pseudo-proper lifetime distributions of the measured dimuons, with mass in the 3.0–3.2GeV window. The vertical lines indicate the “prompt” (dashed) and “non-prompt” (dotted) windows.

event distributions, for the data and for the MC.

Figure 12-left shows the  $J/\psi |\cos \theta|$  vs.  $p_T$  event distribution measured with the 2018 event sample, for the Peak region, after applying all the event selection criteria. In this kind of ”2D map” representation, the analogous distributions for the NP region and for the 2017 data taking period are virtually indistinguishable from the one shown here. The corresponding MC distribution, for the

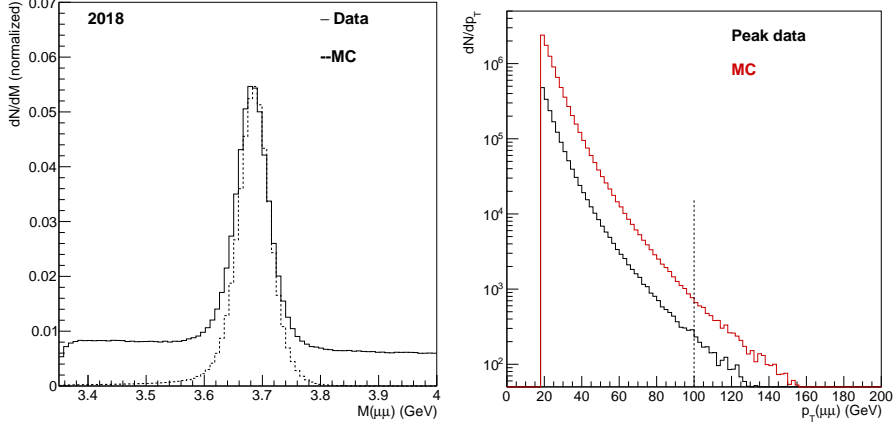


Figure 10: Left: Invariant mass distribution of the measured (solid histogram) and simulated (dashed histogram) prompt dimuons ( $|c\tau| < 50 \mu\text{m}$ ), integrated over  $p_T$ . Right: Measured (black) and simulated (red)  $p_T$  distributions of the dimuons in the prompt  $\psi(2S)$  signal region ( $|c\tau| < 50 \mu\text{m}$  and  $3.57 < m < 3.81 \text{ GeV}$ ).

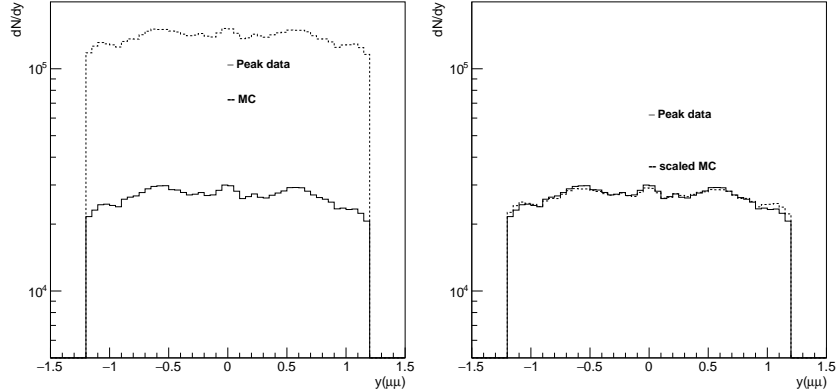


Figure 11: Rapidity distributions of the measured (solid) and simulated (dashed) prompt dimuons in the  $\psi(2S)$  mass region, integrated over  $p_T$ , before (left) and after (right) rescaling the MC distributions for an easier comparison with the data shapes.

2018 conditions, is shown in Fig. 12-right. Since the MC samples are generated unpolarized, the non-flatness of this distribution versus  $|\cos \theta|$  is a direct reflection of the detection acceptance. The measured data, instead, is also affected by the physics polarization effects that we are interested in measuring.

Besides the expected (exponential) decrease in event yields as  $p_T$  increases, which simply reflects the decreasing  $p_T$ -differential production cross section,

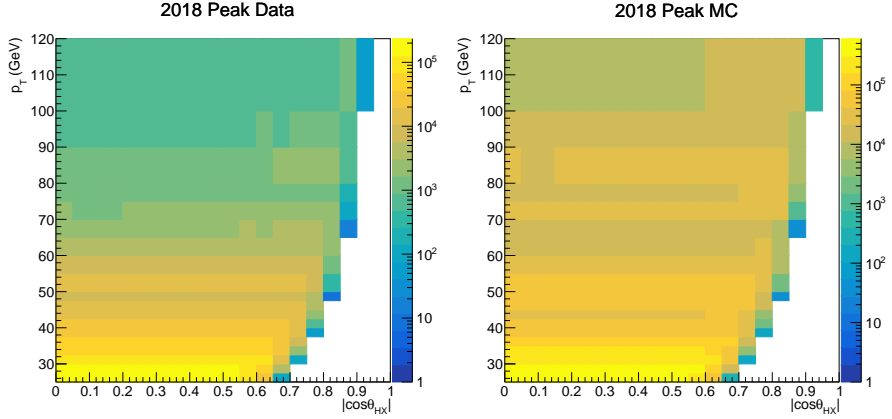


Figure 12: Two-dimensional  $J/\psi$  ( $|\cos\theta|, p_T$ ) distributions for 2018 Peak data (left) and signal-only MC (right).

the first observation that we can make from these figures is that the coverage in  $|\cos\theta|$  extends to larger values when the dimuons have a larger  $p_T$ . In fact, the requirement that *both* muons must have  $p_T > 5.6$  GeV implies that we cannot see in our sample any events where the two muons are “back-to-back” in the helicity frame, blinding us from seeing the  $\cos\theta$  regions close to  $-1$  or  $+1$ . As the dimuon  $p_T$  increases, the impact of the muon  $p_T$  cut becomes less important, so that we see the measured  $|\cos\theta|$  distribution extending towards higher values of  $|\cos\theta|$ , as shown in Fig. 13. In other words, the maximum value of the  $|\cos\theta|$  variable that we can probe in our data increases with dimuon  $p_T$ , which is another good reason to perform the analysis as a function of  $p_T$ .

It is worth noting that this means that the polarization measurement becomes easier to perform as the  $J/\psi$   $p_T$  increases (as long as we do not “run out of events”). Indeed, the measurement of  $\lambda_\theta$  benefits very significantly from the shape of the  $\cos\theta$  distribution *away from zero*. Data that only cover a  $\cos\theta$  range very close to zero are unable to provide a faithful measurement of  $\lambda_\theta$ .

Before acceptance-corrections, all the measured  $\cos\theta$  distributions (in the HX frame) decrease towards the edges,  $|\cos\theta| \rightarrow 1$ . If we would fit them immediately with Eq. 3, we would probably get negative  $\lambda_\theta$  values, especially at low dimuon  $p_T$ , even if the  $J/\psi$  mesons would be produced unpolarized or with transverse polarization. As mentioned before, the analysis must be made using the data over MC ratios. Figure 14 shows an example of such a ratio, for the Peak region, using the 2018 data and MC  $J/\psi$  samples. The detection effects cancel in the ratio, so that its study will provide a reliable measurement of the polarizations. Indeed, the polarization is the only effect that is present in the measured distributions and not in the simulated ones, so that it is the only possible cause of the (potential) non-flatness of the ratios.

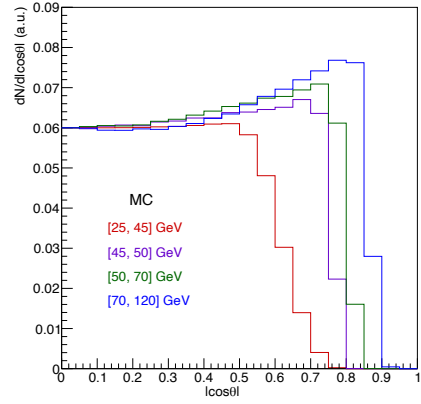


Figure 13: Simulated  $|\cos \theta|$  distributions, in four  $J/\psi$   $p_T$  ranges, showing that the  $|\cos \theta|$  coverage increases with  $p_T$ .

Figure 15 shows the equivalent, for the  $\psi(2S)$  events, of the panels shown in Figs. 12 and 14.

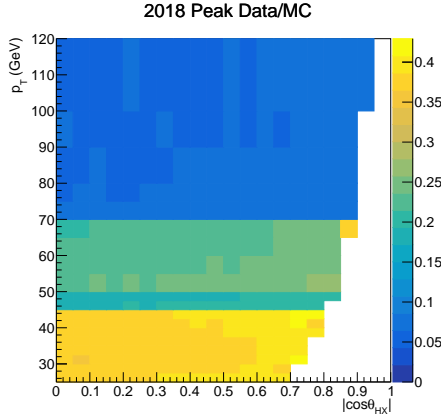


Figure 14: Data over MC ratio of the  $J/\psi$  ( $|\cos \theta|, p_T$ ) 2D distributions for the Peak region, using the 2018 samples.

To ensure stable and reliable fit results, the  $1 + \lambda_\theta \cos^2 \theta$  function is fitted within a  $|\cos \theta|$  range that excludes the most extreme values, where the distribution (corrected for acceptance and efficiency effects) is the ratio of two steeply falling distributions and, hence, might be affected by spurious “edge effects”.

Before we go into more complex descriptions of the analysis procedures, it is worth noting that, even without doing any fits, a direct look at the measured  $J/\psi$   $|\cos \theta|$  distributions, shown in Fig. 16 for the Peak, NP and MC cases, integrated over  $p_T$ , is sufficient to see that the Peak dimuons are transversely polarized while the NP dimuons, instead, are longitudinally polarized. This observation can be easily made by comparing the Peak and NP shapes with that of the *unpolarized MC* distribution, taken as reference.

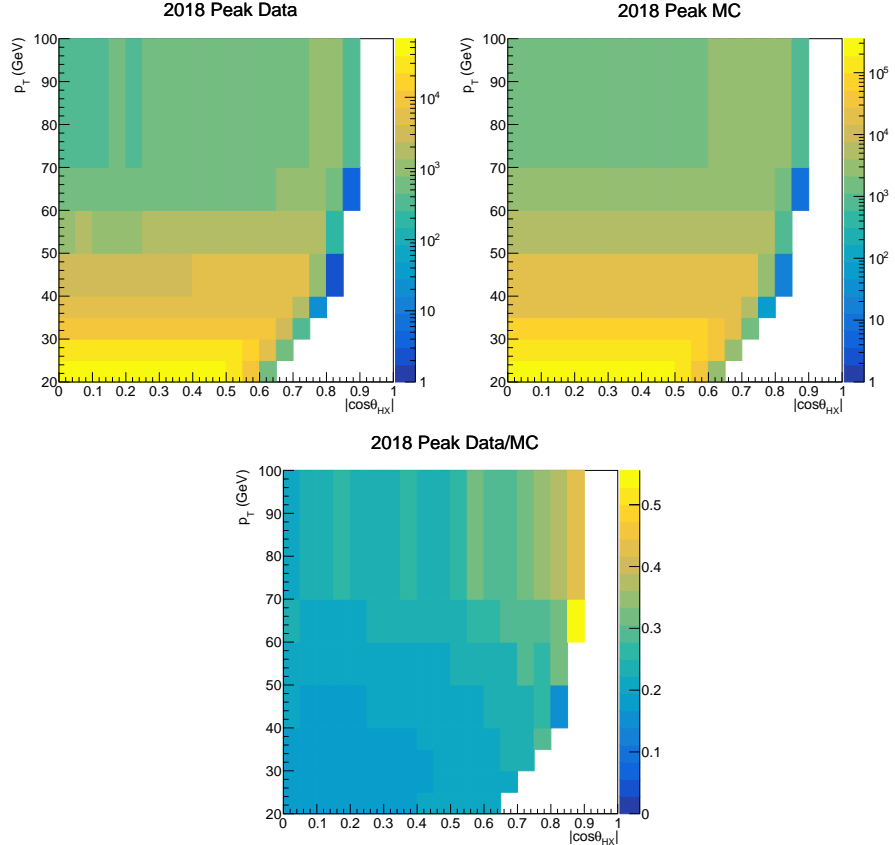


Figure 15: Two-dimensional  $\psi(2S)$  ( $|\cos\theta|, p_T$ ) distributions for 2018 Peak data (top left), signal-only MC (top right), and data over MC ratio (bottom).

Also for pedagogical purposes, we will now illustrate the polarization measurement for the dimuons in the Peak and NP regions, without subtracting any of the background terms. While these are not to be seen as final physics results, they have the advantage of showing, in a simple way, how the procedure translates the angular distributions in the  $\lambda_\theta$  polarization parameter.

Figure 17-left shows the  $|\cos\theta|$  distribution of the 2018 Peak (violet) and NP (red) dimuons, for the 42.5–45 GeV dimuon  $p_T$  bin, an intermediate  $p_T$  bin, suitable for this illustration. As mentioned before, these distributions reflect not only the polarization of the respective dimuons but also the detector acceptance effects. The right-side panel of the same figure shows the ratio between the measured distributions and the simulated one, for the same data taking period and  $p_T$  bin. In these ratios, the detector effects cancel out and we can proceed to the fit step, using the function  $1 + \lambda_\theta \cos^2 \vartheta$ . The results are  $\lambda_\theta = 0.157 \pm 0.016$  for the Peak dimuons and  $\lambda_\theta = -0.178 \pm 0.015$  for the NP dimuons, for this

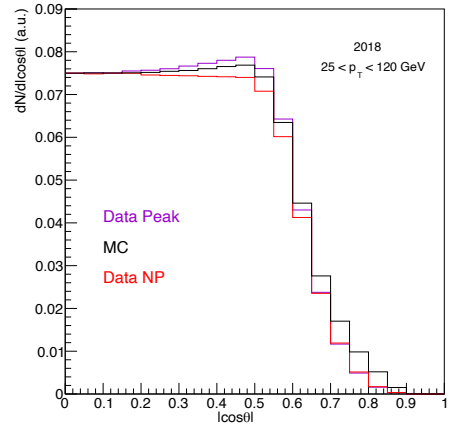


Figure 16: Measured Peak (purple) and NP (red)  $J/\psi |\cos \theta|$  distributions compared to the MC simulated (unpolarized) distribution (black), immediately illustrating the transverse or longitudinal polarizations of the measured samples.

specific  $p_T$  bin, of the 2018 data.

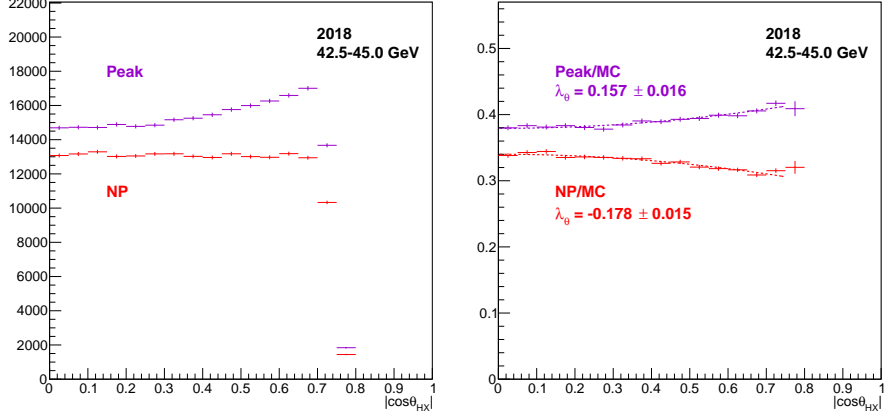


Figure 17: Illustration of the analysis procedure: the Peak and NP  $|\cos \theta|$  distributions (left) and the Peak/MC and NP/MC ratios (right), in the 42.5–45GeV  $p_T$  bin of the 2018 data.

Applying this procedure to all the  $p_T$  bins and to both periods of data taking provides the values of  $\lambda_\theta$  as a function of  $p_T$  shown in Fig. 18.

As previously mentioned, these results are only shown in here because we believe that it is informative to see how the polarization values, vs.  $p_T$ , are obtained from the measured angular distributions, before we proceed into the background subtraction steps.

In particular, the NP  $\lambda_\theta$  values shown in Fig. 18 cannot be seen as measurements of the polarizations of the non-prompt  $J/\psi$  mesons, resulting from  $B$  decays, because the NP event sample is contaminated by non-prompt “mass-continuum” muon pairs that happen to have an invariant mass between 3.0 and 3.2GeV but are not produced by  $J/\psi$  decays. This background contribution needs to be evaluated, using the NP LSB and NP RSB sideband regions mentioned above, and then subtracted, before we achieve the final physics result.

Analogously, the  $\lambda_\theta$  values obtained from the Peak region cannot be interpreted as a measurement of the prompt  $J/\psi$  polarization, because it is affected by the (prompt) mass-continuum muon pairs and also by the  $J/\psi$  mesons produced by  $B$  mesons that decay with a very small lifetime value, so that they are counted in the PR region ( $|ct| < 50\ \mu\text{m}$ ).

Nevertheless, while not yet being physical measurements, these  $\lambda_\theta$  versus  $p_T$  trends offer a useful first approximation of the final results, under the (reasonable) assumption that the backgrounds are relatively small and/or have a negligible impact on the polarization measurement.

In particular, it is interesting to note that the measured values extend over a very broad  $p_T$  range and have uncertainties that are much smaller than those we have seen in the analysis of the 7TeV data (Fig. 1).

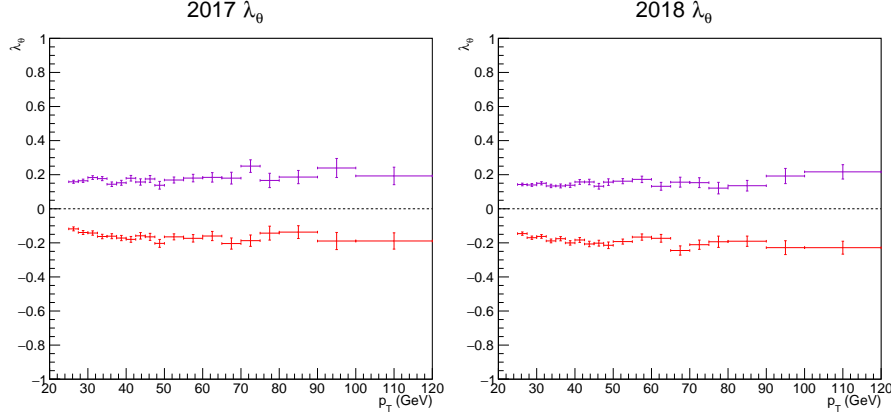


Figure 18: Illustration of the analysis procedure: the  $\lambda_\theta$  values measured for the Peak (violet) and NP (red) dimuons collected in 2017 (left) and 2018 (right), before subtracting the background contributions.

The next step is to measure the  $\lambda_\theta$  polarization parameter of the *signal* prompt and non-prompt  $J/\psi$  and  $\psi(2S)$  mesons. For simplicity, we will describe the procedures for the  $J/\psi$  case; the  $\psi(2S)$  measurement is done in the same way. For the prompt case, and as just mentioned, we must subtract from the Peak sample two sources of background: the underlying mass continuum background caused by (uncorrelated) muon pairs, evaluated by integrating, inside the  $J/\psi$  peak region, the continuum distribution defined by the left and right sidebands; and the  $J/\psi$  mesons resulting from decays of  $B$  mesons, evaluated by integrating, inside the PR region, the lifetime distribution of the NP term, defined by the NP region. This background subtraction must be done, naturally, as a function of  $p_T$ . The procedure is represented by the following equation:

$$\begin{aligned} \text{Peak}(|\cos\theta|, p_T) = & (1 - f_{\text{NP}}(p_T) - f_{\text{Bg}}(p_T)) \cdot \psi_{\text{PR}}(|\cos\theta|, p_T) \\ & + f_{\text{NP}}(p_T) \cdot \text{NP}(|\cos\theta|, p_T) \\ & + f_{\text{Bg}}(p_T) \cdot \text{Bg}(|\cos\theta|, p_T). \end{aligned} \quad (5)$$

Or, equivalently, by:

$$\begin{aligned} \psi_{\text{PR}}(|\cos\theta|, p_T) = & \frac{1}{1 - f_{\text{NP}}(p_T) - f_{\text{Bg}}(p_T)} \times \\ & [\text{Peak}(|\cos\theta|, p_T) - f_{\text{NP}}(p_T) \cdot \text{NP}(|\cos\theta|, p_T) - f_{\text{Bg}}(p_T) \cdot \text{Bg}(|\cos\theta|, p_T)]. \end{aligned} \quad (6)$$

In order to determine the physically-relevant  $\psi_{\text{PR}}(|\cos\theta|, p_T)$  term from the immediately measurable  $\text{Peak}(|\cos\theta|, p_T)$  term, we need to evaluate the  $\text{NP}(|\cos\theta|, p_T)$  and  $\text{Bg}(|\cos\theta|, p_T)$  distributions, as well as the fractions of

events in the Peak region which are due to these two sources,  $f_{\text{NP}}(p_T)$  and  $f_{\text{Bg}}(p_T)$ . We do that through the analysis of the dimuon mass and lifetime distributions, presented in the next chapter.

The procedure for the measurement of the signal non-prompt  $J/\psi$  polarization is analogous but simpler because there is only one background term, the (non-prompt) continuum muon pairs:

$$\begin{aligned} \text{NP}(|\cos\theta|, p_T) = & (1 - f_{\text{NPBg}}(p_T)) \cdot \psi_{\text{NP}}(|\cos\theta|, p_T) \\ & + f_{\text{NPBg}}(p_T) \cdot \text{NPBg}(|\cos\theta|, p_T). \end{aligned} \quad (7)$$

The Peak( $|\cos\theta|, p_T$ ) and NP( $|\cos\theta|, p_T$ ) distributions are directly obtained from the measured event samples. The Bg( $|\cos\theta|, p_T$ ) and NPBg( $|\cos\theta|, p_T$ ) distributions are evaluated as a weighted average of the (PR or NP) LSB and RSB samples. The fractions of background contributions,  $f_{\text{Bg}}$  and  $f_{\text{NP}}$ , are determined by fitting the dimuon mass and lifetime distributions, respectively. Figure 19 provides a graphical illustration of these two backgrounds.

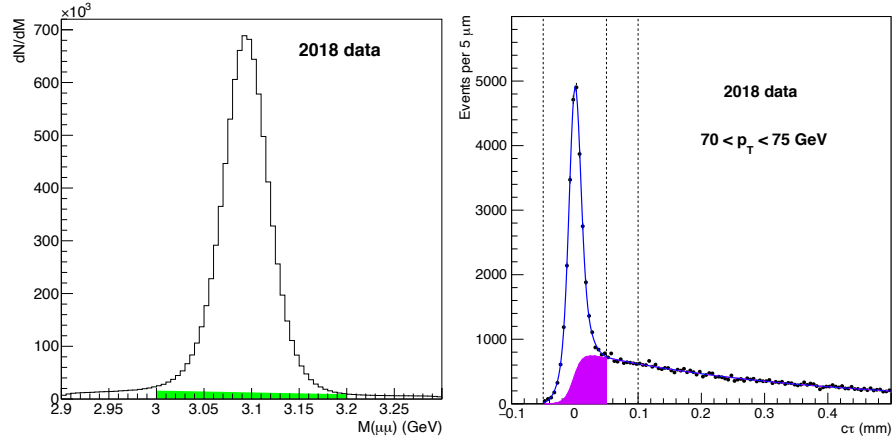


Figure 19: Examples of measured dimuon mass and lifetime distributions, using the 2018  $J/\psi$  sample, meant to illustrate the shape and magnitude of the mass and lifetime backgrounds under the prompt  $J/\psi$  peak.

Before we move on to the study of the dimuon mass and lifetime distributions, we should clarify that we have done several comparisons between the 2017 and 2018 samples, including independent fits of the dimuon mass and lifetime distributions of each of those samples, and arrived at the conclusion that the two samples lead to distributions that are in perfect agreement with each other, within uncertainties. This observation means that we can perform the dimuon mass and lifetime fits using the combined “Run 2” event sample. In this way, some free parameters can be fitted with less statistical fluctuations and we can see more precisely if they depend or not on the dimuon  $p_T$ , for example.

Residual variations between the two event samples, if any, are covered by assigning systematic uncertainties evaluated from the differences between the results independently obtained for each year. This applies, independently, to the prompt and non-prompt  $J/\psi$  and  $\psi(2S)$  measurements.

Adding both years, the event yields, per 2D region and  $p_T$  range, are collected in the Tables 4 and 5, for the  $J/\psi$  and  $\psi(2S)$  cases, respectively.

Table 4: Event yields of the measured and simulated  $J/\psi$  samples, adding the 2017 and 2018 sets, per  $p_T$  range (in GeV).

|      |                                 | 2017 | [25, 45] | [45, 50] | [50, 70] | [70, 120] | [25, 120] |
|------|---------------------------------|------|----------|----------|----------|-----------|-----------|
| Data | Prompt signal region (Peak)     |      | 13.362 M | 0.517 M  | 0.698 M  | 0.180 M   | 14.757 M  |
|      | Non-prompt region (NP)          |      | 9.629 M  | 0.445 M  | 0.626 M  | 0.168 M   | 10.869 M  |
|      | Prompt left mass SB (PRLSB)     |      | 113.8 k  | 5.2 k    | 7.7 k    | 2.4 k     | 129.2 k   |
|      | Prompt right mass SB (PRRSB)    |      | 132.4 k  | 7.3 k    | 11.3 k   | 4.0 k     | 155.0 k   |
|      | Non-prompt left mass SB (NPLSB) |      | 159.1 k  | 7.4 k    | 10.2 k   | 2.8 k     | 179.5 k   |
|      | Non-prompt right mass SB (NPRS) |      | 168.1 k  | 8.0 k    | 11.0 k   | 3.0 k     | 190.0 k   |
| MC   | only Peak region                |      | 41.492 M | 3.145 M  | 3.759 M  | 2.874 M   | 51.270 M  |

Table 5: Event yields of the measured and simulated  $\psi(2S)$  samples, adding the 2017 and 2018 sets, in the full  $p_T$  range.

|      |                                 | 2017 | [20, 100] |
|------|---------------------------------|------|-----------|
| Data | Prompt signal region (Peak)     |      | 2.130 M   |
|      | Non-prompt region (NP)          |      | 1.351 M   |
|      | Prompt left mass SB (PRLSB)     |      | 404.8 k   |
|      | Prompt right mass SB (PRRSB)    |      | 459.5 k   |
|      | on-prompt left mass SB (NPLSB)  |      | 367.6 k   |
|      | Non-prompt right mass SB (NPRS) |      | 141.6 k   |
| MC   | only Peak region                |      | 10.349 M  |

## 4 Dimuon mass and lifetime dimensions

As we have seen in the previous chapter, the measurement of the  $\lambda_\theta$  polarization parameter of the prompt (or non-prompt)  $J/\psi$  (or  $\psi(2S)$ ) mesons is made

by fitting the ratio between the corresponding measured and simulated two-dimensional ( $|\cos\theta|, p_T$ ) distributions. While the MC distribution is already the needed one (only the signal is simulated), the measured distribution needs to be computed by subtracting the relevant background terms from the directly measured distribution (Eqs. 5 and 7).

We will report in this chapter our studies of the mass and lifetime dimensions, leading to the evaluation of the needed 2D ( $|\cos\theta|, p_T$ ) distributions and of the corresponding fractions, as functions of  $p_T$ .

#### 4.1 The dimuon mass distribution

For simplicity, the analysis is only described for the  $J/\psi$  case, but it applies in an analogous way for the  $\psi(2S)$  case.

The dimuon mass distribution is described by the superposition of a double Crystal-Ball function plus a Gaussian function to describe the  $J/\psi$  signal line shape ( $L_\psi$ ) and a decreasing exponential function to describe the underlying mass continuum background ( $L_{Bg}$ ):

$$L_\psi = f_{CB_1} \cdot g_{CB_1}(m) + (1 - f_{CB_1} - f_G) \cdot g_{CB_2}(m) + f_G \cdot g_G(m) \quad (8)$$

$$L_{Bg} = N_{Bg} \exp(-m/t_{Bg}) \quad (9)$$

The fraction  $f_{Bg}$  of events in the Peak region corresponding to ‘‘continuum muon pairs’’ is computed by integrating the  $L_{Bg}$  function in the 3.0–3.2 GeV mass window and then dividing the result by the total number of events counted in that mass range.

The two CB functions have common means,  $\mu_m$ , and tail parameters,  $n$  and  $\alpha$ , and independent widths,  $\sigma_{CB_1}$  and  $\sigma_{CB_2}$ . The Gaussian function has the same mean,  $\mu_m$ , and an independent width,  $\sigma_G$ .

Independently fitting the dimuon mass distributions in each of the 19  $p_T$  bins would naturally lead to results affected by random statistical fluctuations, especially if all shape parameters would be left free. We know that some of the parameters are (anti-)correlated and it is not reasonable to leave them all free in the fit (that is the case, in particular, of the  $n$  and  $\alpha$  tail parameters). We also know that the shape parameters of the  $L_\psi$  and  $L_{Bg}$  functions must change with  $p_T$  in a smooth way.

After a series of preliminary studies of the (simulated and measured) dimuon mass distributions, we converged on a fit model that is able to faithfully describe the data with a relatively small number of free shape parameters, determined from the *simultaneous* fit of the 19 mass distributions, either as constants or as linear functions of  $p_T$ . We think that this relatively simple model represents a good balance between having too many free parameters (leading to under-constrained fits and results affected by random statistical fluctuations) and having too many arbitrarily-selected constraints (possibly leading to results biased by our specific assumptions).

The fit model used for the  $J/\psi$  analysis is constrained as follows:

- $\mu_m$ ,  $f_{CB_1}$  and  $\alpha$  are independent of  $p_T$ ;
- $\sigma_{CB_1}$ ,  $\sigma_{CB_2}$  and  $\sigma_G$  are linear functions of  $p_T$  with a common slope;
- $f_G = 3.5\%$  and  $n = 2.5$ .

The only difference in the  $\psi(2S)$  fit model is that we set  $f_G = 2.5\%$  instead of 3.5%. We have seen, however, that this very small term could even be simply neglected, as it has no effect at all on the results of the analysis (we only include it to avoid non-negligible pulls on the right side tail of the  $J/\psi$ ).

The inverse slopes of the mass continuum exponential function,  $t_{Bg}$ , are left free in all  $p_T$  bins. This is the most important shape parameter of the dimuon mass fits, for the purpose of our analysis, given that all we need from these fits is the fraction  $f_{Bg}$ , versus  $p_T$ .

The fitted  $t_{Bg}$  values are shown in Fig. 20, for the  $J/\psi$  (left) and  $\psi(2S)$  (right) analyses.

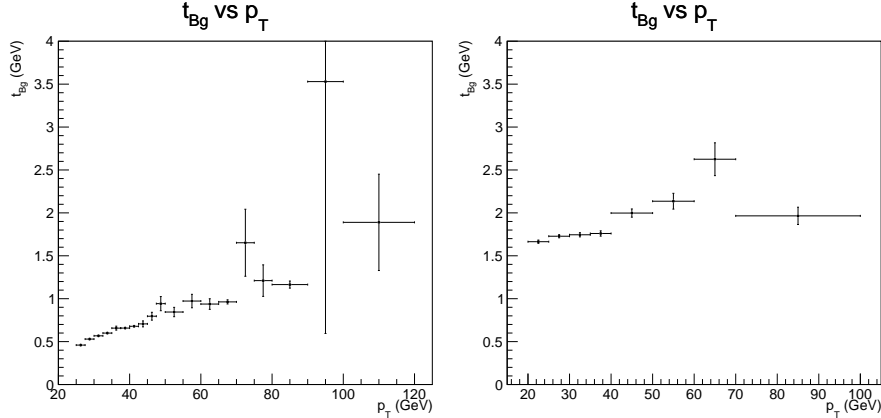


Figure 20: Fitted  $t_{Bg}$  versus  $p_T$ , for the  $J/\psi$  (left) and  $\psi(2S)$  (right) analyses.

The measured mass distributions are well described by the fit model; there are no systematic trends in the pull distributions. Figure 21 illustrates the fit quality in the  $J/\psi$  case, for two typical  $p_T$  bins.

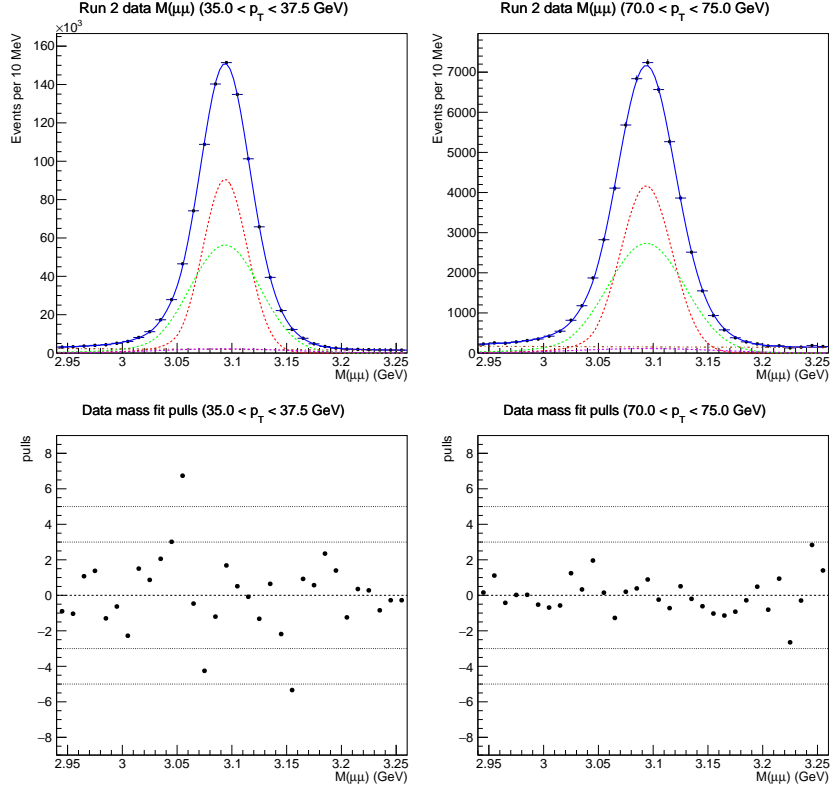


Figure 21: Fitted  $J/\psi$  mass distributions for two  $p_T$  bins (top) and corresponding pull distributions (bottom).

Figures 22 and 23 show the corresponding plots for the  $\psi(2S)$ , respectively for the prompt and non-prompt cases.

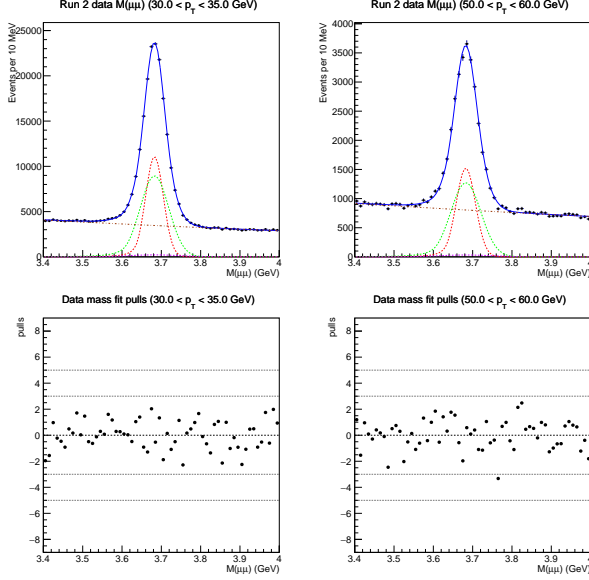


Figure 22: Fitted prompt  $\psi(2S)$  mass distributions for two  $p_T$  bins (top) and corresponding pull distributions (bottom).

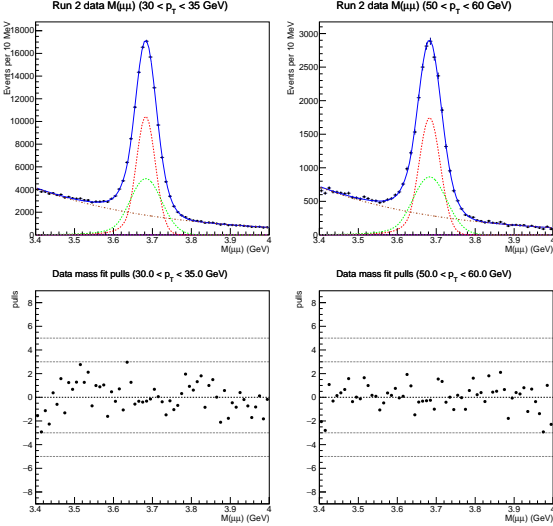


Figure 23: Fitted non-prompt  $\psi(2S)$  mass distributions for two  $p_T$  bins (top) and corresponding pull distributions (bottom).

As mentioned before, the fraction of mass continuum muon pairs in the Peak window,  $f_{\text{Bg}}$ , is evaluated (in each  $p_T$  bin) by integrating the fitted background function in that window and dividing the result by the total number of events in that window. The results are shown in Fig. 24, for the prompt and non-prompt  $\text{J}/\psi$  and  $\psi(2\text{S})$  analyses.

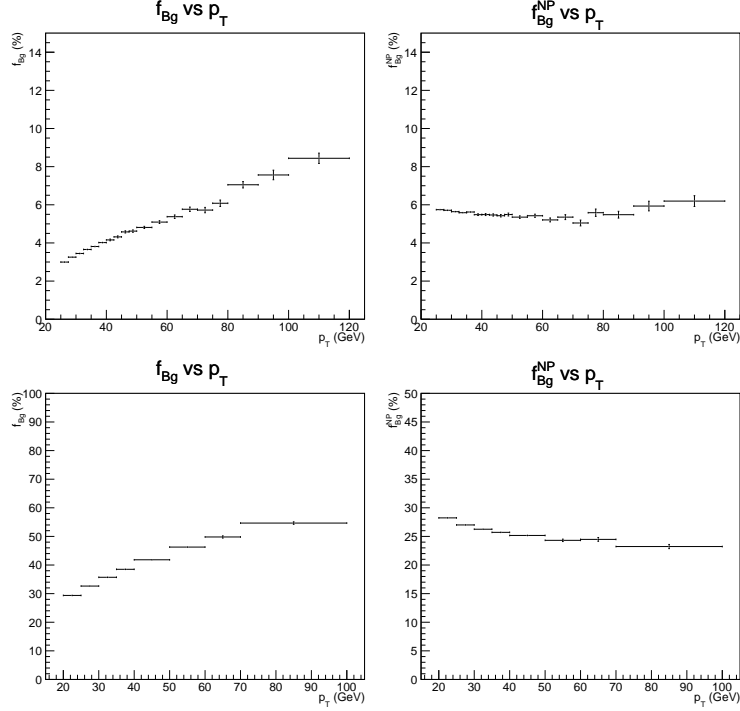


Figure 24: Measured  $f_{\text{Bg}}$  fractions vs.  $p_T$ , for the prompt (left) and non-prompt (right)  $\text{J}/\psi$  (top) and  $\psi(2\text{S})$  (bottom) analyses.

## 4.2 The dimuon lifetime distribution

The dimuon lifetime distribution, in the window from  $-50$  to  $+500 \mu\text{m}$ , is described by the superposition of two terms: the prompt and non-prompt contributions.

The PR term is, effectively, the lifetime resolution function. Given that we are considering a sample of events integrated over rapidity, and knowing that the lifetime resolution is not independent of rapidity, it is reasonable to assume that the resolution function should be the convolution of many Gaussian functions. In practice, the sum of only two Gaussian functions already provides a sufficiently-good description of the data, at least for our purposes:

$$L_{\text{PR}} \equiv L_{\text{res}} = f_{G_1} \times G_1(c\tau|\mu_{c\tau}, \sigma_{G_1}) + (1 - f_{G_1}) \times G_2(c\tau|\mu_{c\tau}, \sigma_{G_2}). \quad (10)$$

The two Gaussian functions share the same mean,  $\mu_{c\tau}$ , but have independent widths,  $\sigma_{G_1}$  and  $\sigma_{G_2}$ . We define the Gaussian  $G_1$  (the one that contributes the fraction  $f_{G_1}$ ) as being the narrower of the two.

The NP term is parametrized as a decreasing exponential for  $c\tau > 0$  convolved with the resolution function just introduced:

$$L_{\text{NP}} = [\exp(-c\tau/t_{\text{NP}}) \times \mathcal{H}(c\tau)] \otimes L_{\text{res}}(c\tau|\mu_{c\tau}, \sigma_{G_1}, \sigma_{G_2}), \quad (11)$$

where  $\mathcal{H}$  is the Heaviside step function.

The fraction of events in the prompt region that are due to  $J/\psi$  mesons produced in  $B$  decays,  $f_{\text{NP}}$ , is evaluated (in each  $p_T$  bin) by integrating the fitted  $L_{\text{NP}}$  function in the PR window,  $|c\tau| < 50 \mu\text{m}$ , and then dividing the result by the total number of events in that region.

As we did for the definition of the dimuon mass fit model, we started by performing a series of preliminary studies, including the option of independently fitting each of the 19 lifetime distributions, in the region  $[-50, 500] \mu\text{m}$ , with all the shape parameters free. As expected, we see that this option leads to a fit with too much freedom, as shown by the correlated fluctuations of the parameters  $f_{G_1}$ ,  $\sigma_{G_1}$  and  $\sigma_{G_2}$ . We also see that  $\mu_{c\tau}$  is clearly independent of  $p_T$ , as shown in Fig. 25-left. So, we proceed with a simultaneous fit of the 19 distributions imposing that the  $\mu_{c\tau}$  and  $f_{G_1}$  parameters are independent of  $p_T$ . The resulting  $\sigma_{G_1}$  and  $\sigma_{G_2}$  values show a much smoother variation with  $p_T$ , as shown in Fig. 25-right.

The inverse slope of the  $J/\psi$  NP exponential function,  $t_{NP}$ , is essentially the same in both fitting options, as we can easily see in Fig. 26. This is the most important shape parameter of the dimuon lifetime fits, for the purpose of our analysis, given that all we need from these fits is the fraction  $f_{NP}$ , versus  $p_T$ .

The analogous plots for the  $\psi(2S)$  case are shown in Fig. 27.

The measured lifetime distributions are well described by the fit model; there are no systematic trends in the pull distributions. Figures 28 and 29 illustrate the fit quality in the  $J/\psi$  and  $\psi(2S)$  cases, respectively, for two typical  $p_T$  bins.

As mentioned earlier, the fraction of events in the prompt (“Peak”) region that are due to  $J/\psi$  (or  $\psi(2S)$ ) mesons produced in  $B$  decays,  $f_{NP}$ , is evaluated (in each  $p_T$  bin) by integrating the fitted  $L_{NP}$  function in that window and then dividing the result by the total number of Peak events. The results are shown in Fig. 30, for the  $J/\psi$  and  $\psi(2S)$  analyses. As expected from previous analyses, the  $J/\psi$  “non-prompt fraction” increases with  $p_T$  and then saturates. The results are identical when the  $\mu_{c\tau}$  and  $f_{G_1}$  parameters are left free (black points) or are common to all  $p_T$  bins (red points).

Knowing the fractions of non-prompt  $J/\psi$  (or  $\psi(2S)$ ) mesons and continuum muon pairs in the Peak region, we can deduce the corresponding fraction of prompt  $J/\psi$  (or  $\psi(2S)$ ) mesons. The results are shown in Fig. 31, for the  $J/\psi$  and  $\psi(2S)$  analyses.

### 4.3 An interesting side remark

We conclude this chapter with an interesting side remark: the *shape* of the  $p_T$  dependence of the background contamination functions can be determined without any fits. Indeed, it is sufficient to compute the ratios between the event yields counted in the NP or mass sideband regions and the Peak region. Figure 32 shows, using the  $J/\psi$  example, that this trivial alternative procedure gives virtually the same trends vs.  $p_T$ .

## 5 Polarization measurement

In the previous chapter we have described the procedure to get the fractions of background events, both from the dimuon mass continuum in the NP and PR signal regions ( $f_{Bg}$ ) and from the “non-prompt” mesons in the PR signal region ( $f_{NP}$ ). We have also presented the results, as a function of  $p_T$ .

As shown in Eqs. 5 and 7, the measurement of the prompt ( $\psi_{PR}(|\cos\theta|, p_T)$ ) and non-prompt ( $\psi_{NP}(|\cos\theta|, p_T)$ ) 2D distributions also implies knowing the  $(|\cos\theta|, p_T)$  2D distributions of the background terms,  $NP(|\cos\theta|, p_T)$  and  $Bg(|\cos\theta|, p_T)$ .

The NP term is easy to get, simply building the  $(|\cos\theta|, p_T)$  distribution of the events in the NP region:  $100 < c\tau < 500 \mu\text{m}$  and  $3.0 < m < 3.2 \text{GeV}$  ( $J/\psi$ ) or  $3.57 < m < 3.81 \text{GeV}$  ( $\psi(2S)$ ).

We have verified that the  $(|\cos\theta|, p_T)$  distribution does not show any significant variations with lifetime, within the range  $100\text{--}500 \mu\text{m}$ , so that we can trust the “extrapolation” to the prompt region.

The dimuon mass continuum  $Bg$  term is obtained by interpolating, for each  $p_T$  bin, the  $|\cos\theta|$  distributions of the mass sidebands into the signal mass region. The interpolation is done as a weighted average of the two SB distributions:

$$f_L(p_T) \cdot \text{LSB}(|\cos\theta|, p_T) + (1 - f_L(p_T)) \cdot \text{RSB}(|\cos\theta|, p_T), \quad (12)$$

where, for the  $J/\psi$  case,

$$f_L = \frac{3.1 \text{GeV} - \langle m_{LSB} \rangle}{\langle m_{RSB} \rangle - \langle m_{LSB} \rangle} \quad (13)$$

and

$$\langle m_{LSB, RSB} \rangle = \left\{ \int_{m_{\min}}^{m_{\max}} m \cdot f_{Bg}(m) dm \right\} / \left\{ \int_{m_{\min}}^{m_{\max}} f_{Bg}(m) dm \right\}. \quad (14)$$

In the  $\psi(2S)$  case, the value  $3.1 \text{GeV}$  is replaced by  $3.69 \text{GeV}$ . The weight  $f_L$  is found to be essentially independent of  $p_T$  and slightly above 50%, for both states.

Figures 33 and 34 show the LSB, RSB, and interpolated (weighted average)  $|\cos \theta|$  distributions for the  $J/\psi$  and  $\psi(2S)$  cases, respectively, in two  $p_T$  bins and for the PR and NP samples.

As mentioned before, we determine the non-prompt  $J/\psi$  and  $\psi(2S)$   $|\cos\theta|$  distributions, as a function of  $p_T$ , by subtracting from the NP sample the non-prompt mass continuum background, using the  $|\cos\theta|$  distributions interpolated from the sidebands, just discussed, and the background fractions presented in the previous chapter.

Figure 35-left shows the  $|\cos\theta|$  distributions of the  $J/\psi$  NP events (in black) and of the mass-continuum background events (in green, scaled by its fraction), as well as their difference, the non-prompt  $J/\psi$   $|\cos\theta|$  distribution (in red), for one illustrative  $p_T$  bin. Figure 35-right shows the ratio between the measured and simulated distributions, before and after subtracting the mass-continuum term. The legends in the figure give the values of  $\lambda_\theta$  obtained from the fits of these ratios, for this specific  $p_T$  bin.

Repeating the same procedure for all  $p_T$  bins we obtain the  $p_T$ -dependence of the  $\lambda_\theta$  parameter, shown in Fig. 36 for the  $J/\psi$  and  $\psi(2S)$  cases. The two sets of points show the measurements before and after the subtraction of the underlying dimuon mass continuum.

An almost identical procedure has been followed to measure the polarizations of the prompt  $J/\psi$  and  $\psi(2S)$  mesons. The only difference is that we also need to subtract the fraction of events in the PR window that are actually the result of B meson decays, even though they have small  $c\tau$  values. We actually subtract the non-prompt *signal* distributions, after subtracting the non-prompt sidebands background, rather than the NP distributions, to avoid subtracting twice the dimuon mass continuum events.

Figure 37-left shows the  $|\cos \theta|$  distributions of the several terms, similarly to what was previously shown in Fig. 35. The prompt events in the  $J/\psi$  mass region (Peak) are shown in violet; the two background sources, scaled by their corresponding fractions, are shown in green (mass continuum) and in red (non-prompt  $J/\psi$  signal). Subtracting the red points from the violet ones we get the black points (PR). Finally, subtracting the green points from the black ones gives us the prompt  $J/\psi$  signal, shown in blue.

The right panel of Fig. 37 shows the ratios between the measured and the simulated  $|\cos \theta|$  distributions, together with the  $\lambda_\theta$  values resulting from their fits.

As done before for the non-prompt case, we obtain the  $p_T$ -dependence of the  $\lambda_\theta$  parameter by repeating the same procedure for all  $p_T$  bins. The results are shown in Fig. 38 for the  $J/\psi$  and  $\psi(2S)$  cases, with several sets of points, corresponding to the terms previously mentioned.

Before moving on to the study of the systematic uncertainties of these measurements, in the next chapter, it is useful to have a look at the present results, directly comparing the  $J/\psi$  and  $\psi(2S)$  cases in a single figure. This is done in Fig. 39.

## 6 Systematic uncertainties

In this chapter we present and evaluate the systematic uncertainties associated to the polarization measurements reported in the previous chapter.

After considering several potential sources of systematic uncertainties, we converged on the following list, which will be discussed in detail in the next sections.

- Potential differences between the 2017 and 2018 samples;
- Fit model of the dimuon mass distributions;
- Single muon detection efficiencies;
- Dimuon detection efficiencies (“ $\rho$  factor”);
- Potential residual azimuthal anisotropy in the helicity frame.

### 6.1 Potential differences between the 2017 and 2018 samples

To study the impact of possible differences between the 2017 and 2018 event samples, we measured the prompt  $J/\psi$  polarization independently in each sample. As can be seen in Fig. 40, for the  $J/\psi$  and  $\psi(2S)$  cases, the two measurements are compatible with each other, within their (independent) statistical uncertainties. We could consider this to be a “passed check” but, to be conservative, we will assign a systematic uncertainty of  $\pm 0.012$ , independent of  $p_T$ , to this effect. This uncertainty is represented in the figures by the pink band.

## 6.2 Fit model of the dimuon mass distributions

The  $J/\psi$  line shape does not enter directly in the determination of the fraction of mass continuum muon pairs in the signal region, 3.0–3.2GeV, because we use, as denominator, the number of counted events. Besides, the signal function (two Crystal-Ball functions plus one Gaussian function) has enough freedom to adapt to the measured data, without biasing the fit of the continuum background. The same arguments apply, naturally, to the  $\psi(2S)$  analysis.

The biggest source of uncertainty comes from the fact that we impose an exponential function for the description of the continuum background. To evaluate the potential impact of this choice we have redone the  $\lambda_\theta$  measurement replacing the exponential by a linear function. The new results are virtually identical to the baseline values. Therefore, no uncertainty is assigned to these effects.

It is worth noting that the low-mass edge of the LSB windows, both for the  $J/\psi$  and  $\psi(2S)$  cases, were set to higher values than allowed by the trigger to avoid edge effects.

Figure 41 shows, for illustration, the variation of  $\lambda_\theta$  for the  $J/\psi$  and  $\psi(2S)$  analyses, when the mass continuum background is fitted with a linear function, with respect to the baselines values.

### 6.3 Single muon detection efficiencies

The single muon  $p_T$  cut of 5.6GeV ensures that all the selected events have muons of similar detection efficiencies (in the plateau), so that an inaccurate parametrization of the efficiency curve will have a negligible impact on the results. For the muons in the region  $|\eta| < 0.2$ , however, the “turn-on region” is not completely removed, as can be seen in Fig. 42.

We considered two checks to evaluate if the results might be affected by a potentially wrong efficiency correction of the events in this  $\eta$  region.

- **Efficiency curve reweighting:**

We take the single muon efficiency function for this  $\eta$  range,

$$f(p_T) = \frac{1}{1 + \exp[-\beta \cdot (p_T - p_{T0})]} \quad (\beta = 1.698, \quad p_{T0} = 3.723)$$

and consider two extreme cases:

- 1) There is no inefficiency at all: we weigh the MC events by  $1/f(p_T)$ ;
- 2) The real efficiency differs from the MC efficiency by an amount equal to the efficiency itself: we weigh the MC events by  $f(p_T)$ .

- **$p_T$  cut:**

We increase the  $p_T$  cut from 5.6 to 6.7GeV for the muons with  $|\eta| < 0.2$ , completely removing their turn-on region.

The differences between the  $\lambda_\theta$  values obtained in each of these three alternative analyses and those of the baseline analysis are shown in Fig. 43, for the  $J/\psi$  (left) and  $\psi(2S)$  (right) analyses, together with a grey band centred at zero that represents the statistical uncertainty of the baseline results.

We assign a systematic uncertainty from this source, up to 50GeV for the  $J/\psi$  and up to 40GeV for the  $\psi(2S)$ , computed (conservatively) as the average of the absolute differences between each of the two reweighting options and the baseline values.

The muons produced with pseudorapidity in the  $0.2 < |\eta| < 0.3$  region have a lower muon detection efficiency because of the gap between the central wheel and its neighbours. To evaluate the possible impact of a miscorrection of this efficiency, we measured  $\lambda_\theta$  after rejecting all events with a muon (or both) in this  $\eta$  region. As shown in Fig. 44 for the  $J/\psi$  and  $\psi(2S)$  analyses, the difference between the varied and baseline  $\lambda_\theta$  values, vs.  $p_T$ , is randomly distributed around zero; the deviations seem to be purely statistical. Therefore, we do not assign a systematic uncertainty to this source.

## 6.4 Dimuon detection efficiencies (“ $\rho$ factor”)

The dimuon efficiency is smaller than the product of the two single muon efficiencies, due to trigger-induced muon-pair correlations that become significant at high  $p_T$ :

$$\epsilon_{\mu\mu} = \epsilon_{\mu,1} \cdot \epsilon_{\mu,2} \cdot \rho. \quad (15)$$

In principle, this effect should be faithfully reproduced by the detailed trigger emulation, included in the MC simulation, but it is important to evaluate if our results could be affected by some residual differences. Our study follows exactly the same procedure as used in the BPH-13-003 analysis (“Measurement of the prompt  $J/\psi$  and  $\psi(2S)$  polarizations in  $pp$  collisions at  $\sqrt{s} = 7\text{TeV}$ ”); all the details are explained in detail in the [analysis note AN-13-016](#).

The dimuon trigger efficiency is studied by comparing the MC event distributions obtained after applying the trigger (“trig”) to those obtained before (“reco”). We restrict our study to  $p_T > 50\text{GeV}$  events, where the effects are more visible. As can be seen in Fig. 45, the trig/reco ratio of the  $\Delta\phi$  vs.  $\Delta\eta$  2D distribution shows that the trigger efficiency is very low when the two muons are “too close to each other” in the variable  $\Delta R = \sqrt{\Delta\phi^2 + \Delta\eta^2}$ .

The dimuon trigger efficiency depends also on the difference between the  $p_T$  of the two muons,  $\Delta p_T$ , and it is easier to isolate and reject regions of low dimuon efficiency if we apply cuts on the variable  $\Delta R_{p_T}$ , defined as

$$\Delta R_{p_T} = \sqrt{\Delta\phi^2 + \Delta\eta^2} + \frac{\log |\Delta p_T|}{b} \quad (b = 45). \quad (16)$$

Figure 46-left shows that rejecting events of  $\Delta R_{p_T} < 0.17$  leads to a  $J/\psi$  event sample where all the dimuons have trigger efficiency above 70%, so that we are much less sensitive to the accuracy of the MC efficiency correction. Figure 46-right shows the  $p_T$  vs.  $\Delta R_{p_T}$  2D event distribution before applying the trigger emulation (the denominator of the ratio shown on the left panel). We can see that a  $\Delta R_{p_T} < 0.17$  cut rejects a very large fraction of the high- $p_T$  events. Therefore, for  $p_T > 70\text{GeV}$  we use a looser cut,  $\Delta R_{p_T} = 0.15$  (corresponding to an efficiency threshold of 60%), to avoid losing too many events (otherwise the  $\lambda_\theta$  measurement becomes too uncertain to provide meaningful results).

Since the  $\Delta R_{p_T}$  cuts reduce the  $|\cos\theta|$  coverage, we also recompute the baseline  $\lambda_\theta$  fitting the  $|\cos\theta|$  distribution in the same range, to ensure that potential variations are exclusively caused by the  $\rho$  factor.

Figure 47 shows the differences between the  $\lambda_\theta$  values measured with the event sample selected by the  $\Delta R_{p_T}$  cuts, where the dimuon detection efficiency is always quite high, so that we are not too sensitive to the accuracy of the trigger emulation in the simulated events, and the values measured without applying such a cut. We do not see any significant variation of  $\Delta\lambda_\theta$  with  $p_T$ ; the fluctuations around zero are caused by the reduction in the size of the event sample (they are not seen when we use a coarser  $p_T$  binning, as shown by the red points on the  $J/\psi$  panel). Therefore, we consider this a passed check and assign no systematic uncertainty to the measurement from this source.

## 6.5 Potential residual azimuthal anisotropy in the helicity frame

The analysis has been redone, in exactly the same way, replacing the  $|\cos\theta|$  polar angle by the  $\varphi$  azimuthal angle, in the same  $p_T$  bins, etc.

The  $\varphi$  distributions, corrected for acceptance in the same way as previously explained, are then fitted with the function

$$W(\varphi|\vec{\lambda}) \propto 1 + \beta \cos 2\varphi, \quad (17)$$

where  $\beta = (2\lambda_\varphi) / (3 + \lambda_\theta)$ .

The fitted values of  $\beta$ , for both the prompt and non-prompt  $J/\psi$  and  $\psi(2S)$  mesons, are very close to zero, as can be seen in Fig. 48.

Therefore, the acceptance correction can be made in  $|\cos\theta|$ , integrating over the  $\varphi$  angle, neglecting residual correlations between the two angles. It is worth noting that small non-zero  $\beta$  values cannot be considered as evidence that there are residual differences between the acceptance maps evaluated through the MC simulations and the real acceptance maps of the actual detector. In other words, even a perfect MC simulation can lead to acceptance-corrected distributions that exhibit small azimuthal anisotropies in the HX frame. The reason is that we are using the *proton-proton* HX frame and not the *parton-parton* HX frame, that would be more suitable to measure the prompt  $J/\psi$  polarization. Similarly, the  $B$  meson frame would be more suitable to measure the polarization of non-prompt  $J/\psi$  mesons. Since we have no access to those “natural” frames, we must report the measurements in the proton-proton HX frame, where small azimuthal anisotropies can be expected, even if they are absent in the ideal frames.

Nevertheless, to be conservative, we take the extreme approach of considering that the residual non-flatness of the  $\varphi$  distributions is caused by a mismatch between MC and data. Hence, based on our estimates for the  $\beta$  ranges, we compute new  $|\cos\theta|$  vs.  $p_T$  acceptance maps reweighing each MC event by the weight  $1 + \beta \cdot \cos(2\varphi)$ , which depends on the  $\varphi$  of the event.

The differences between the  $\lambda_\theta$  values obtained with the alternative maps (in two extreme options represented by the bands in Fig. 48) and those of the baseline analysis are shown in Fig. 49, for the prompt (top) and non-prompt (bottom)  $J/\psi$  (left) and  $\psi(2S)$  (right) analyses. They are negligible with respect to the grey bands, which represent the statistical uncertainty of the baseline results, so that we could consider this to be a passed check. Nevertheless, we assign a systematic uncertainty from this source, up to 37.5GeV for the  $J/\psi$  case and 35GeV for the  $\psi(2S)$ , computed from the difference between the  $\lambda_\theta$  values obtained with the most extreme  $\beta$  scenario and the baseline values. This uncertainty is asymmetric but it is quite small so that we will retain symmetric total systematic uncertainties.

## 6.6 Summary of the systematic uncertainties

All the uncertainties described in the previous sections of this chapter are summed in quadrature to give the total systematic uncertainty of the measurements. The squared uncertainties are stacked on the positive hemispheres of Fig. 50, where they can be easily compared with the squared statistical uncertainties, shown on the negative hemispheres. This figure shows the results for the non-prompt (left) and prompt (right)  $J/\psi$  (top) and  $\psi(2S)$  (bottom) measurements.

We see that the statistical uncertainties dominate everywhere except for  $p_T$  smaller than  $\sim 50\text{GeV}$  for the  $J/\psi$  polarization measurements.

The numerical values of all uncertainties are collected in Tables 6–9.

Table 6: Systematic uncertainties affecting the prompt  $J/\psi$  polarization measurement.

| $p_T$ (GeV) | years       | $\mu$ eff.  | $\beta$ | total       |
|-------------|-------------|-------------|---------|-------------|
| 25–27.5     |             | $\pm 0.011$ | -0.004  | $\pm 0.017$ |
| 27.5–30     |             | $\pm 0.008$ | -0.003  | $\pm 0.015$ |
| 30–32.5     |             | $\pm 0.007$ | -0.003  | $\pm 0.014$ |
| 32.5–35     |             | $\pm 0.006$ | -0.002  | $\pm 0.013$ |
| 35–37.5     |             | $\pm 0.005$ | -0.002  | $\pm 0.013$ |
| 37.5–40     |             | $\pm 0.004$ | —       | $\pm 0.013$ |
| 40–42.5     |             | $\pm 0.004$ | —       | $\pm 0.013$ |
| 42.5–45     |             | $\pm 0.003$ | —       | $\pm 0.012$ |
| 45–47.5     |             | $\pm 0.002$ | —       | $\pm 0.012$ |
| 47.5–50     | $\pm 0.012$ | $\pm 0.001$ | —       | $\pm 0.012$ |
| 50–55       |             | —           | —       | $\pm 0.012$ |
| 55–60       |             | —           | —       | $\pm 0.012$ |
| 60–65       |             | —           | —       | $\pm 0.012$ |
| 65–70       |             | —           | —       | $\pm 0.012$ |
| 70–75       |             | —           | —       | $\pm 0.012$ |
| 75–80       |             | —           | —       | $\pm 0.012$ |
| 80–90       |             | —           | —       | $\pm 0.012$ |
| 90–100      |             | —           | —       | $\pm 0.012$ |
| 100–120     |             | —           | —       | $\pm 0.012$ |

## 7 Results

The final results of this analysis are displayed in Fig. 51, which shows the  $\lambda_\theta$  parameters for the prompt and non-prompt  $J/\psi$  and  $\psi(2S)$  mesons, with the vertical bars representing the statistical and systematic uncertainties summed in quadrature.

The numerical values of these results are collected in Tables 10–13.

Table 7: Systematic uncertainties affecting the non-prompt  $J/\psi$  polarization measurement.

| $p_T$ (GeV) | years       | $\mu$ eff.  | $\beta$  | total       |
|-------------|-------------|-------------|----------|-------------|
| 25–27.5     |             | $\pm 0.011$ | $+0.005$ | $\pm 0.017$ |
| 27.5–30     |             | $\pm 0.008$ | $+0.003$ | $\pm 0.015$ |
| 30–32.5     |             | $\pm 0.007$ | $+0.004$ | $\pm 0.014$ |
| 32.5–35     |             | $\pm 0.006$ | $+0.002$ | $\pm 0.013$ |
| 35–37.5     |             | $\pm 0.005$ | $+0.002$ | $\pm 0.013$ |
| 37.5–40     |             | $\pm 0.004$ | —        | $\pm 0.013$ |
| 40–42.5     |             | $\pm 0.004$ | —        | $\pm 0.013$ |
| 42.5–45     |             | $\pm 0.003$ | —        | $\pm 0.012$ |
| 45–47.5     |             | $\pm 0.002$ | —        | $\pm 0.012$ |
| 47.5–50     | $\pm 0.012$ | $\pm 0.001$ | —        | $\pm 0.012$ |
| 50–55       |             | —           | —        | $\pm 0.012$ |
| 55–60       |             | —           | —        | $\pm 0.012$ |
| 60–65       |             | —           | —        | $\pm 0.012$ |
| 65–70       |             | —           | —        | $\pm 0.012$ |
| 70–75       |             | —           | —        | $\pm 0.012$ |
| 75–80       |             | —           | —        | $\pm 0.012$ |
| 80–90       |             | —           | —        | $\pm 0.012$ |
| 90–100      |             | —           | —        | $\pm 0.012$ |
| 100–120     |             | —           | —        | $\pm 0.012$ |

## 8 Summary

The prompt and non-prompt  $J/\psi$  and  $\psi(2S)$   $\lambda_\theta$  polarization parameters have been measured, in the helicity frame, using a sample of pp collisions at  $\sqrt{s} = 13\text{TeV}$  collected in 2017 and 2018, corresponding to an integrated luminosity of  $103.3 \text{ fb}^{-1}$ . The results cover a very broad  $p_T$  range, extending up to  $p_T$  values around  $100\text{GeV}$ .

Figure 52 compares the prompt  $J/\psi$  and  $\psi(2S)$   $\lambda_\theta$  measurements obtained in this analysis, with the results previously published by CMS, corresponding to pp collisions at  $\sqrt{s} = 7\text{TeV}$  collected in 2011 [5] (and already shown in Fig. 1). Figure 53 shows only the  $J/\psi$  measurements, for improved visibility.

Table 8: Systematic uncertainties affecting the prompt  $\psi(2S)$  polarization measurement.

| $p_T$ (GeV) | years       | $\mu$ eff.  | $\beta$ | total       |
|-------------|-------------|-------------|---------|-------------|
| 20–25       |             | $\pm 0.014$ | -0.010  | $\pm 0.021$ |
| 25–30       |             | $\pm 0.008$ | -0.006  | $\pm 0.016$ |
| 30–35       |             | $\pm 0.005$ | -0.004  | $\pm 0.013$ |
| 35–40       | $\pm 0.012$ | $\pm 0.001$ | —       | $\pm 0.012$ |
| 40–50       |             | —           | —       | $\pm 0.012$ |
| 50–60       |             | —           | —       | $\pm 0.012$ |
| 60–70       |             | —           | —       | $\pm 0.012$ |
| 70–100      |             | —           | —       | $\pm 0.012$ |

Table 9: Systematic uncertainties affecting the non-prompt  $\psi(2S)$  polarization measurement.

| $p_T$ (GeV) | years       | $\mu$ eff.  | $\beta$ | total       |
|-------------|-------------|-------------|---------|-------------|
| 20–25       |             | $\pm 0.014$ | +0.013  | $\pm 0.023$ |
| 25–30       |             | $\pm 0.008$ | +0.007  | $\pm 0.016$ |
| 30–35       |             | $\pm 0.005$ | +0.004  | $\pm 0.014$ |
| 35–40       | $\pm 0.012$ | $\pm 0.001$ | —       | $\pm 0.012$ |
| 40–50       |             | —           | —       | $\pm 0.012$ |
| 50–60       |             | —           | —       | $\pm 0.012$ |
| 60–70       |             | —           | —       | $\pm 0.012$ |
| 70–100      |             | —           | —       | $\pm 0.012$ |

It is interesting to note that the 7TeV measurements, albeit with large uncertainties, show  $\lambda_\theta$  values that are closer to zero, in the 10–20GeV  $p_T$  range, than those we have measured in this analysis, at higher  $p_T$ , for both the  $J/\psi$  and  $\psi(2S)$  results. As indicated by the dashed red line in Fig. 53, the values of  $\lambda_\theta$  show a steady increase as  $p_T$  increases.

We see no evidence of strong transverse polarizations, even at  $p_T$  values around 30 times the  $J/\psi$  mass. In the NRQCD language, we do not see evidence that, at very high  $p_T$ , the transversely polarized  $^3S_1^{[8]}$  octet term becomes dominant with respect to the unpolarized  $^1S_0^{[8]}$  octet.

These results provide important constraints to be included in global analyses of quarkonium production.

## References

- [1] Brilcalc documentation. CMS internal documentation available at <http://cms-service-lumi.web.cern.ch/cms-service-lumi;brilwsdoc.html>, 2015.

Table 10:  $\lambda_\theta$  parameter measured in the HX frame, as a function of  $p_T$ , for the prompt  $J/\psi$  mesons.

| $p_T$ (GeV) | $\lambda_\theta$ | $\sigma_{\text{stat}}$ | $\sigma_{\text{sys}}$ |
|-------------|------------------|------------------------|-----------------------|
| 25–27.5     | 0.179            | $\pm 0.007$            | $\pm 0.017$           |
| 27.5–30     | 0.192            | $\pm 0.008$            | $\pm 0.015$           |
| 30–32.5     | 0.213            | $\pm 0.009$            | $\pm 0.014$           |
| 32.5–35     | 0.206            | $\pm 0.010$            | $\pm 0.013$           |
| 35–37.5     | 0.191            | $\pm 0.012$            | $\pm 0.013$           |
| 37.5–40     | 0.204            | $\pm 0.013$            | $\pm 0.013$           |
| 40–42.5     | 0.228            | $\pm 0.015$            | $\pm 0.013$           |
| 42.5–45     | 0.221            | $\pm 0.017$            | $\pm 0.012$           |
| 45–47.5     | 0.221            | $\pm 0.018$            | $\pm 0.012$           |
| 47.5–50     | 0.224            | $\pm 0.021$            | $\pm 0.012$           |
| 50–55       | 0.245            | $\pm 0.017$            | $\pm 0.012$           |
| 55–60       | 0.264            | $\pm 0.021$            | $\pm 0.012$           |
| 60–65       | 0.227            | $\pm 0.026$            | $\pm 0.012$           |
| 65–70       | 0.275            | $\pm 0.034$            | $\pm 0.012$           |
| 70–75       | 0.292            | $\pm 0.036$            | $\pm 0.012$           |
| 75–80       | 0.205            | $\pm 0.042$            | $\pm 0.012$           |
| 80–90       | 0.233            | $\pm 0.040$            | $\pm 0.012$           |
| 90–100      | 0.344            | $\pm 0.059$            | $\pm 0.012$           |
| 100–120     | 0.300            | $\pm 0.056$            | $\pm 0.012$           |

- [2] S. Agostinelli et al. GEANT4—a simulation toolkit. *Nucl. Instrum. Meth. A*, 506:250, 2003.
- [3] BPH\_PAG. Onia2MuMu package for Run II. Available at [https://github.com/cms-sw/cmssw/tree/CMSSW\\_10\\_6\\_X/HeavyFlavorAnalysis/Onia2MuMu](https://github.com/cms-sw/cmssw/tree/CMSSW_10_6_X/HeavyFlavorAnalysis/Onia2MuMu), 2015.
- [4] Serguei Chatrchyan et al. Measurement of the relative prompt production rate of  $\chi_{c2}$  and  $\chi_{c1}$  in pp collisions at  $\sqrt{s} = 7$  TeV. *Eur. Phys. J. C*, 72:2251, 2012.
- [5] Serguei Chatrchyan et al. Measurement of the prompt  $J/\psi$  and  $\psi'$  polarizations in pp collisions at  $\sqrt{s} = 7$  TeV. *Phys. Lett. B*, 727:381, 2013.
- [6] Serguei Chatrchyan et al. Measurement of the  $\Upsilon(1S)$ ,  $\Upsilon(2S)$ , and  $\Upsilon(3S)$  polarizations in pp collisions at  $\sqrt{s} = 7$  TeV. *Phys. Rev. Lett.*, 110:081802, 2013.
- [7] N. Davidson, T. Przedzinski, and Z. Wąs. PHOTOS interface in C++: technical and physics documentation. *Comput. Phys. Commun.*, 199:86, 2016.

Table 11:  $\lambda_\theta$  parameter measured in the HX frame, as a function of  $p_T$ , for the non-prompt  $J/\psi$  mesons.

| $p_T$ (GeV) | $\lambda_\theta$ | $\sigma_{\text{stat}}$ | $\sigma_{\text{sys}}$ |
|-------------|------------------|------------------------|-----------------------|
| 25–27.5     | −0.141           | ±0.007                 | ±0.017                |
| 27.5–30     | −0.163           | ±0.007                 | ±0.015                |
| 30–32.5     | −0.158           | ±0.008                 | ±0.014                |
| 32.5–35     | −0.180           | ±0.008                 | ±0.013                |
| 35–37.5     | −0.170           | ±0.009                 | ±0.013                |
| 37.5–40     | −0.189           | ±0.010                 | ±0.013                |
| 40–42.5     | −0.182           | ±0.011                 | ±0.013                |
| 42.5–45     | −0.188           | ±0.012                 | ±0.012                |
| 45–47.5     | −0.185           | ±0.013                 | ±0.012                |
| 47.5–50     | −0.208           | ±0.015                 | ±0.012                |
| 50–55       | −0.178           | ±0.011                 | ±0.012                |
| 55–60       | −0.166           | ±0.014                 | ±0.012                |
| 60–65       | −0.162           | ±0.017                 | ±0.012                |
| 65–70       | −0.225           | ±0.021                 | ±0.012                |
| 70–75       | −0.201           | ±0.021                 | ±0.012                |
| 75–80       | −0.173           | ±0.026                 | ±0.012                |
| 80–90       | −0.168           | ±0.023                 | ±0.012                |
| 90–100      | −0.213           | ±0.032                 | ±0.012                |
| 100–120     | −0.212           | ±0.030                 | ±0.012                |

- [8] P. Faccioli, J. Seixas, and V. Knünz. A new procedure for the determination of angular distribution parameters in dilepton vector meson decays. CMS Note AN-2011/535, 2011.
- [9] Pietro Faccioli and Carlos Lourenço. On the polarization of the non-prompt contribution to inclusive  $J/\psi$  production in  $pp$  collisions. *JHEP*, 10:005, 2022.
- [10] Pietro Faccioli, Carlos Lourenço, and Thomas Madlener. From prompt to direct  $J/\psi$  production: new insights on the  $\chi_{c1}$  and  $\chi_{c2}$  polarizations and feed-down contributions from a global-fit analysis of mid-rapidity LHC data. *Eur. Phys. J. C*, 80:623, 2020.
- [11] Pietro Faccioli, Carlos Lourenço, and João Seixas. New approach to quarkonium polarization studies. *Phys. Rev.*, D81:111502(R), 2010.
- [12] Pietro Faccioli, Carlos Lourenço, and João Seixas. Rotation-invariant relations in vector meson decays into fermion pairs. *Phys. Rev. Lett.*, 105:061601, 2010.
- [13] Pietro Faccioli, Carlos Lourenço, João Seixas, and Hermine K. Wöhri. Study of  $\psi'$  and  $\chi_c$  decays as feed-down sources of  $J/\psi$  hadro-production. *JHEP*, 10:004, 2008.

Table 12:  $\lambda_\theta$  parameter measured in the HX frame, as a function of  $p_T$ , for the prompt  $\psi(2S)$  mesons.

| $p_T$ (GeV) | $\lambda_\theta$ | $\sigma_{\text{stat}}$ | $\sigma_{\text{sys}}$ |
|-------------|------------------|------------------------|-----------------------|
| 20–25       | 0.123            | $\pm 0.028$            | $\pm 0.021$           |
| 25–30       | 0.205            | $\pm 0.033$            | $\pm 0.016$           |
| 30–35       | 0.211            | $\pm 0.043$            | $\pm 0.013$           |
| 35–40       | 0.184            | $\pm 0.063$            | $\pm 0.012$           |
| 40–50       | 0.190            | $\pm 0.063$            | $\pm 0.012$           |
| 50–60       | 0.170            | $\pm 0.098$            | $\pm 0.012$           |
| 60–70       | 0.254            | $\pm 0.167$            | $\pm 0.012$           |
| 70–100      | 0.382            | $\pm 0.187$            | $\pm 0.012$           |

Table 13:  $\lambda_\theta$  parameter measured in the HX frame, as a function of  $p_T$ , for the non-prompt  $\psi(2S)$  mesons.

| $p_T$ (GeV) | $\lambda_\theta$ | $\sigma_{\text{stat}}$ | $\sigma_{\text{sys}}$ |
|-------------|------------------|------------------------|-----------------------|
| 20–25       | -0.114           | $\pm 0.031$            | $\pm 0.023$           |
| 25–30       | -0.134           | $\pm 0.028$            | $\pm 0.016$           |
| 30–35       | -0.207           | $\pm 0.031$            | $\pm 0.014$           |
| 35–40       | -0.170           | $\pm 0.042$            | $\pm 0.012$           |
| 40–50       | -0.227           | $\pm 0.037$            | $\pm 0.012$           |
| 50–60       | -0.231           | $\pm 0.050$            | $\pm 0.012$           |
| 60–70       | -0.200           | $\pm 0.081$            | $\pm 0.012$           |
| 70–100      | -0.096           | $\pm 0.078$            | $\pm 0.012$           |

- [14] Pietro Faccioli, Carlos Lourenço, João Seixas, and Hermine K. Wöhri. Towards the experimental clarification of quarkonium polarization. *Eur. Phys. J. C*, 69:657, 2010.
- [15] Chris Ferraioli. *A Probe of Colored Medium Effects on Quarkonia Polarization in  $\sqrt{s} = 7$  TeV pp collisions at CMS*. PhD thesis, University of Maryland, 2017.
- [16] Vardan Khachatryan et al. Measurement of  $J/\psi$  and  $\psi'$  prompt double-differential cross sections in pp collisions at  $\sqrt{s} = 7$ TeV. *Phys. Rev. Lett.*, 114:191802, 2015.
- [17] Vardan Khachatryan et al. Measurement of the production cross section ratio  $\sigma(\chi_{b2}(1P))/\sigma(\chi_{b1}(1P))$  in pp collisions at  $\sqrt{s} = 8$ TeV. *Phys. Lett. B*, 743:383, 2015.
- [18] Vardan Khachatryan et al.  $\Upsilon(nS)$  polarizations versus particle multiplicity in pp collisions at  $\sqrt{s} = 7$  TeV. *Phys. Lett. B*, 761:31, 2016.
- [19] Valentin Knünz. *Measurement of Quarkonium Polarization to Probe QCD at the LHC*. PhD thesis, Vienna, Tech. U., Atominst., 2015.

- [20] Ilse Kratschmer. *Measurements of prompt  $J/\psi$  and  $\psi(2S)$  production and polarization at CMS*. PhD thesis, Vienna, Tech. U., Atominst., 2015.
- [21] Thomas Madlener. *Measurement of the prompt  $\chi_{c1}$  and  $\chi_{c2}$  polarizations at CMS*. PhD thesis, Technische Universität Wien, 2020.
- [22] A. M. Sirunyan et al. Performance of the CMS muon detector and muon reconstruction with proton-proton collisions at  $\sqrt{s} = 13\text{TeV}$ . *JINST*, 13:P06015, 2018.
- [23] Albert M Sirunyan et al. Constraints on the  $\chi_{c1}$  versus  $\chi_{c2}$  polarizations in proton-proton collisions at  $\sqrt{s} = 8\text{TeV}$ . *Phys. Rev. Lett.*, 124:162002, 2020.
- [24] Torbjörn Sjöstrand, Stephen Mrenna, and Peter Skands. A brief introduction to PYTHIA 8.1. *Comp. Phys. Comm.*, 178:852, 2008.

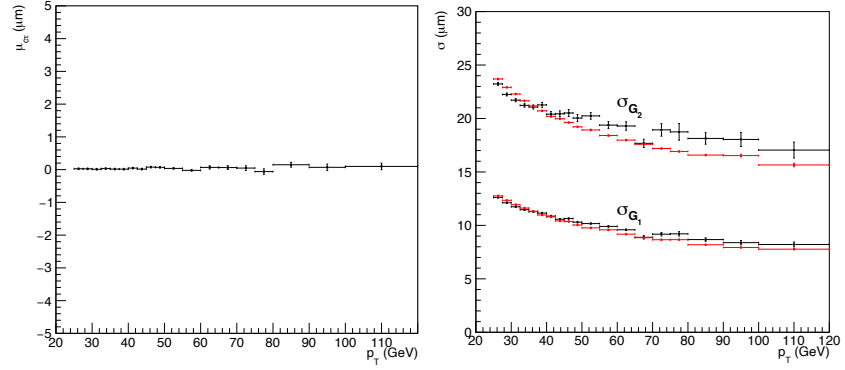


Figure 25: Left:  $J/\psi \mu_{c\tau}$  vs.  $p_T$  when all shape parameters are left free. Right:  $J/\psi \sigma_{G_1}$  and  $\sigma_{G_2}$  vs.  $p_T$ , before (black) and after (red) imposing that the  $\mu_{c\tau}$  and  $f_{G_1}$  parameters are independent of  $p_T$ .

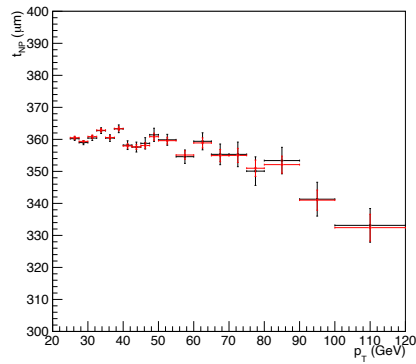


Figure 26: The inverse slope of the NP exponential function,  $t_{NP}$ , as a function of  $p_T$ , when the  $\mu_{c\tau}$  and  $f_{G_1}$  parameters are left free (black) or are constrained to be independent of  $p_T$  (red).

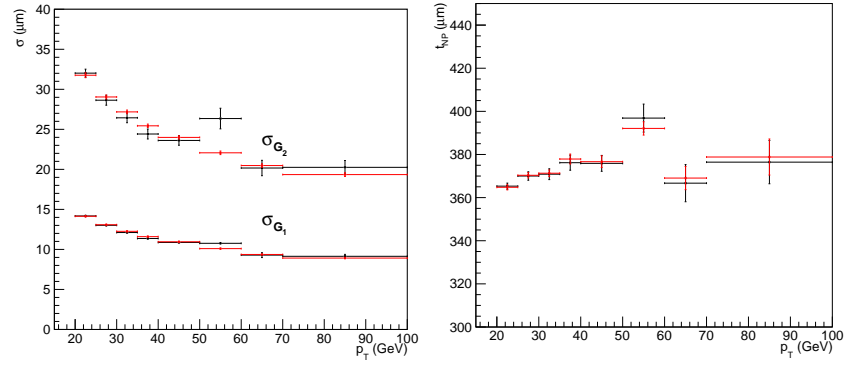


Figure 27: Left:  $\psi(2S)$   $\sigma_{G_1}$  and  $\sigma_{G_2}$  vs.  $p_T$ , before (black) and after (red) imposing that the  $\mu_{ct}$  and  $f_{G_1}$  parameters are independent of  $p_T$ . Right: The inverse slope of the  $\psi(2S)$  NP exponential function,  $t_{NP}$ , as a function of  $p_T$ , when the  $\mu_{ct}$  and  $f_{G_1}$  parameters are left free (black) or are constrained to be independent of  $p_T$  (red).

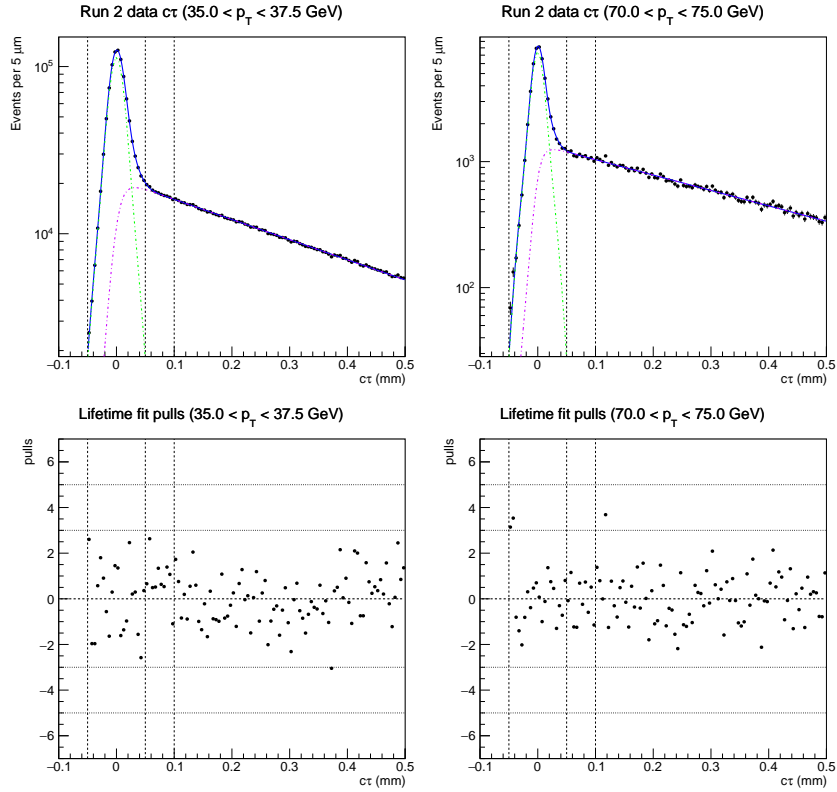


Figure 28: Fitted  $J/\psi$  lifetime distributions for two  $p_T$  bins (top) and corresponding pull distributions (bottom). The vertical black dashed lines mark the limits of the PR and NP regions. The total fit function is shown in blue, while the dash-dotted green and violet lines represent the PR and NP contributions, respectively.

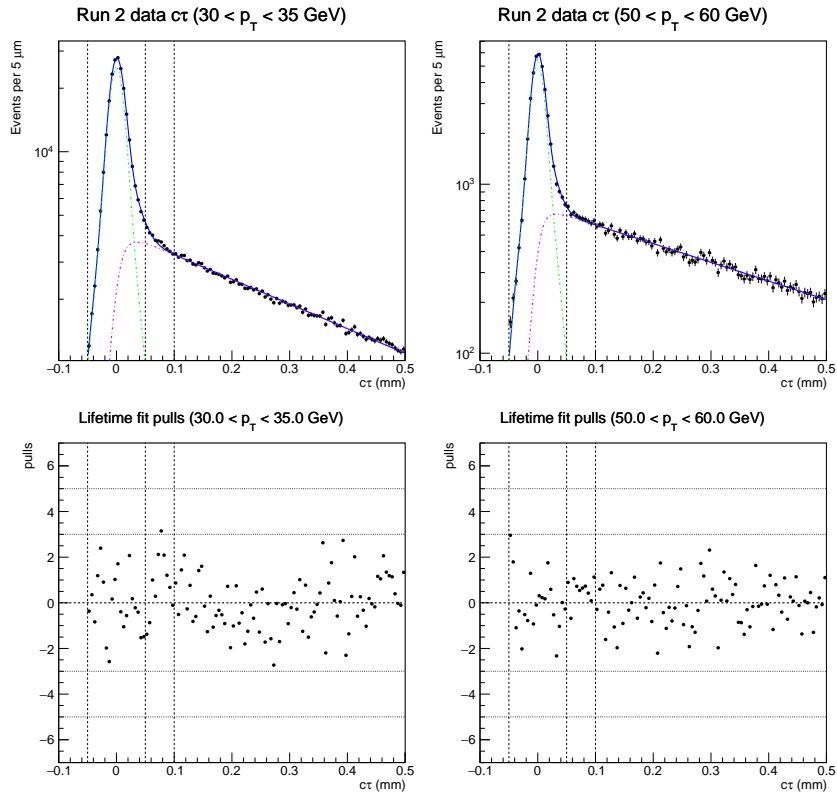


Figure 29: Fitted  $\psi(2S)$  lifetime distributions for two  $p_T$  bins (top) and corresponding pull distributions (bottom). The vertical black dashed lines mark the limits of the PR and NP regions. The total fit function is shown in blue, while the dash-dotted green and violet lines represent the PR and NP contributions, respectively.

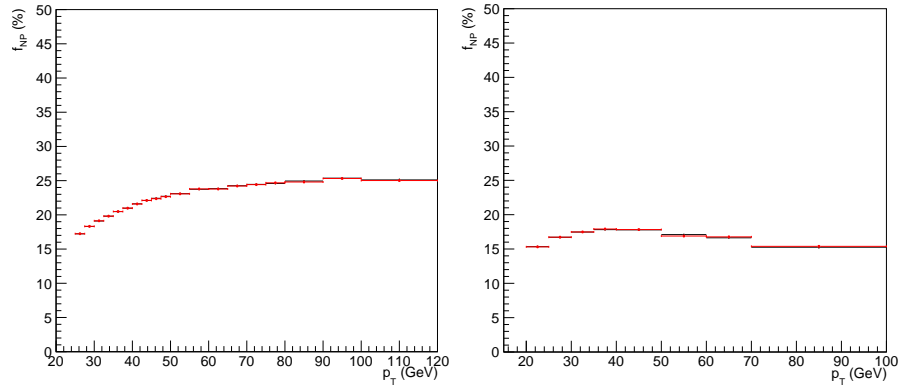


Figure 30: Measured  $f_{NP}$  fractions vs.  $p_T$ , for the  $J/\psi$  (left) and  $\psi(2S)$  (right) analyses.

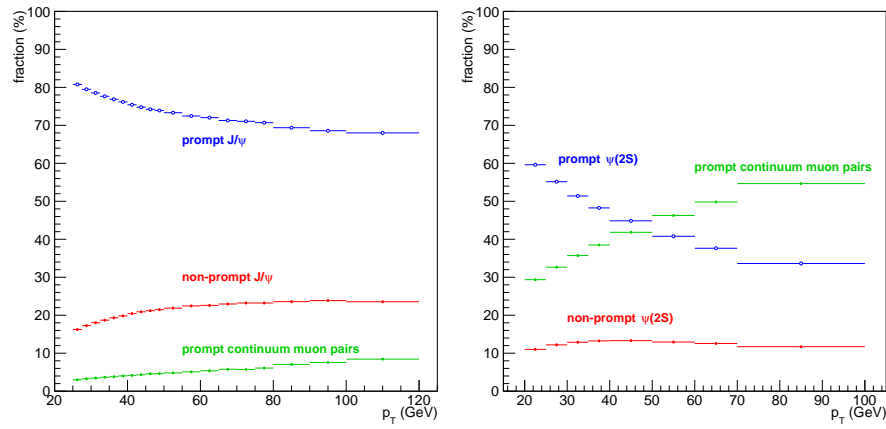


Figure 31: Fractional contributions from each of the three sources of dimuons in the prompt region of the  $J/\psi$  (left) and  $\psi(2S)$  (right) events.

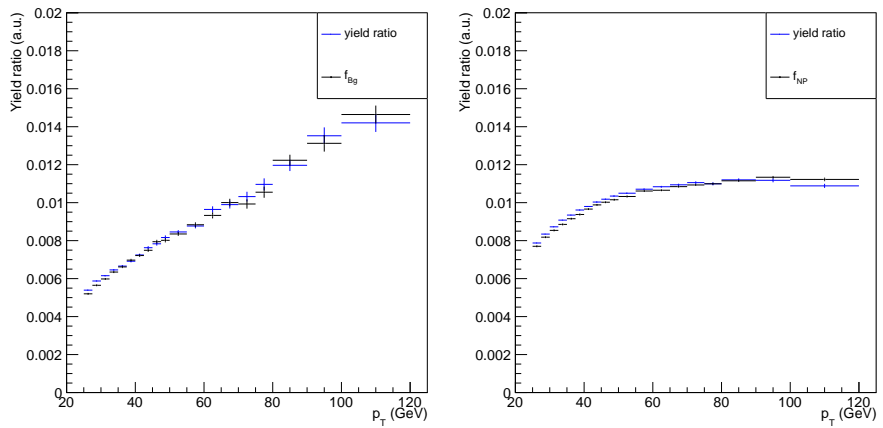


Figure 32: Comparison between the fitted background fractions,  $f_{\text{Bg}}$  (left) and  $f_{\text{NP}}$  (right), with the corresponding ratios of counts, for the  $\text{J}/\psi$  events.

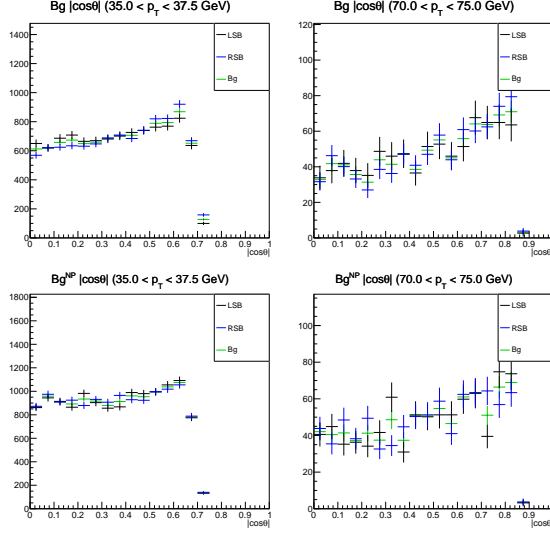


Figure 33: LSB (black), RSB (blue), and interpolated (green)  $|\cos \theta|$  distributions, for two  $p_T$  bins (left and right) in the PR (top) and NP (bottom)  $J/\psi$  samples.

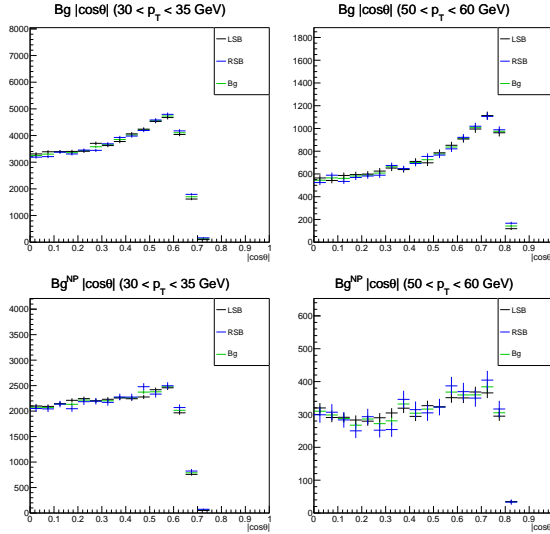


Figure 34: LSB (black), RSB (blue), and interpolated (green)  $|\cos \theta|$  distributions, for two  $p_T$  bins (left and right) in the PR (top) and NP (bottom)  $\psi(2S)$  samples.

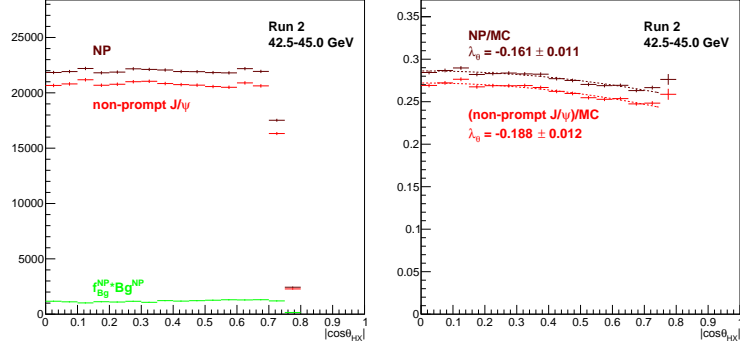


Figure 35: Left:  $|\cos \theta|$  distributions of the NP (brown) and  $Bg$  (green) terms, as well as their difference, the non-prompt  $J/\psi$  signal (red). Right: Ratios between the NP (brown) and non-prompt  $J/\psi$  (red)  $|\cos \theta|$  distributions and the MC distribution for the same  $p_T$  bin.

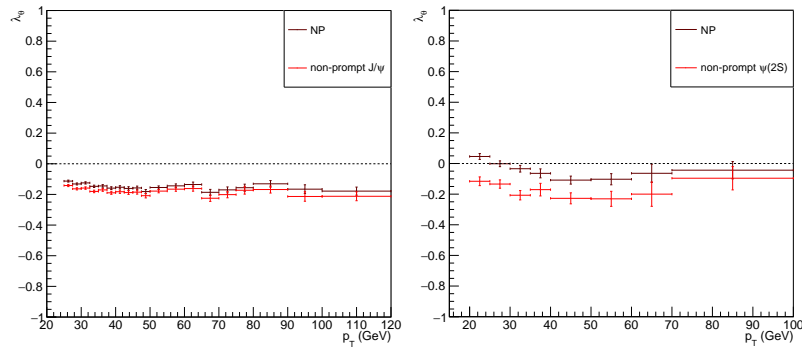


Figure 36: Polarization parameter  $\lambda_\theta$  versus  $p_T$ , measured before (brown) and after (red) subtracting the background from the underlying dimuon mass continuum, for the non-prompt  $J/\psi$  (left) and  $\psi(2S)$  (right) mesons.

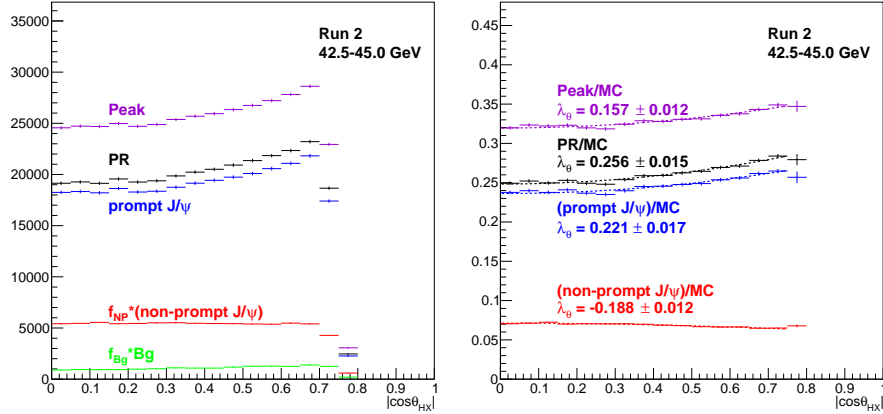


Figure 37: Left:  $|\cos \theta|$  distributions of the Peak events (violet), of the prompt  $J/\psi$  signal (blue), and of the intermediate distributions in the transition from the former to the latter. Right: Ratios between the data and MC  $|\cos \theta|$  distributions, for the same  $p_T$  bin.

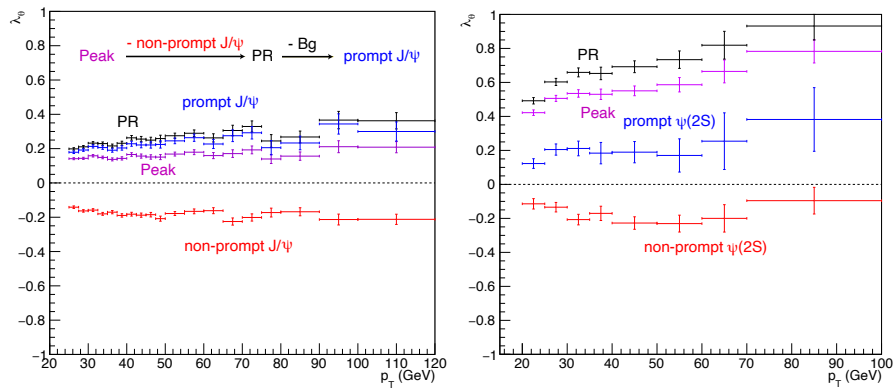


Figure 38: Polarization parameter  $\lambda_\theta$  versus  $p_T$ , measured before and after background subtractions, for the prompt  $J/\psi$  (left) and  $\psi(2S)$  (right) mesons.

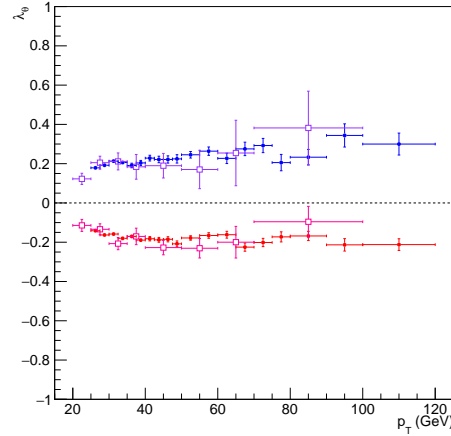


Figure 39: Polarization parameter  $\lambda_\theta$  versus  $p_T$ , for the prompt (blue or purple) and non-prompt (red or magenta)  $J/\psi$  (filled circles) and  $\psi(2S)$  (open squares) mesons.

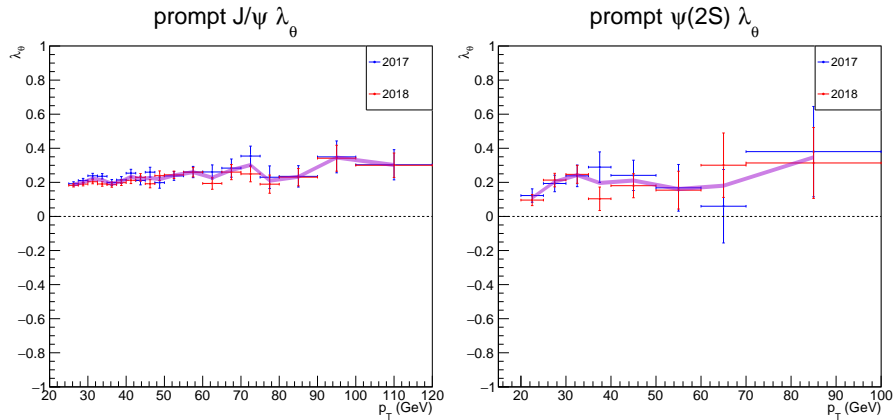


Figure 40:  $\lambda_\theta$  parameter fitted from each of the two years of data taking, for the  $J/\psi$  (left) and  $\psi(2S)$  (right) analyses. The pink band represents a systematic uncertainty of  $\pm 0.012$ .

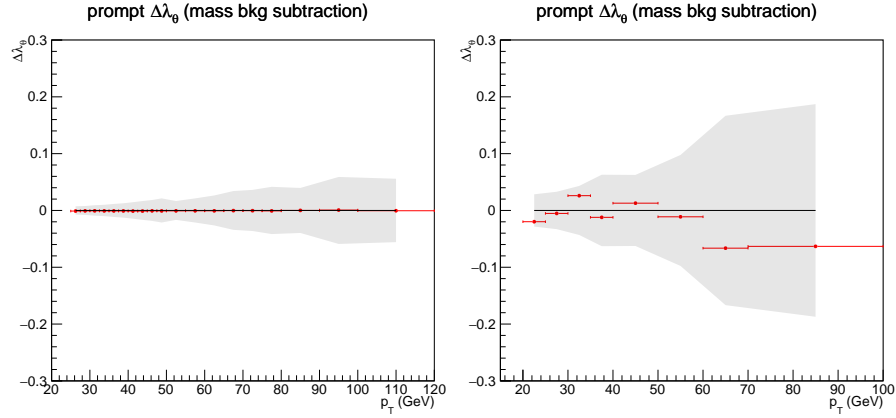


Figure 41: Differences between the  $\lambda_\theta$  values obtained with the varied dimuon mass fit model and the baseline procedure, compared to the statistical uncertainties of the baseline measurement (grey band), for the  $J/\psi$  (left) and  $\psi(2S)$  (right) analyses.

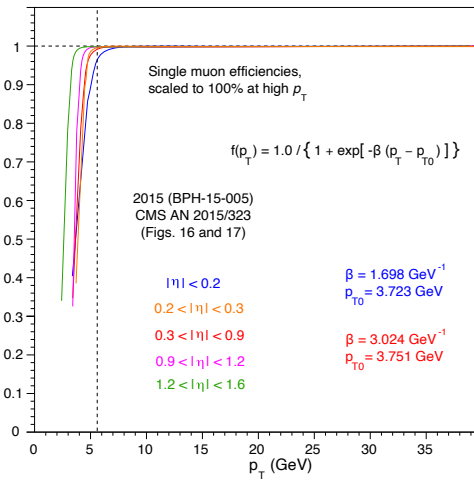


Figure 42: Single muon detection efficiencies for muons in several exclusive  $|\eta|$  bins, as used in the BPH-15-005 cross section measurements.

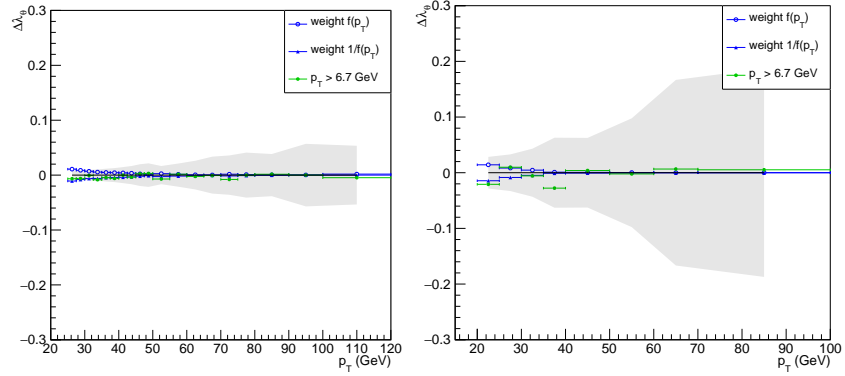


Figure 43: Differences between the  $\lambda_\theta$  values obtained in each of the three alternative analysis scenarios and the baseline procedure, compared to the statistical uncertainties of the baseline measurement (grey band), for the  $J/\psi$  (left) and  $\psi(2S)$  (right) analyses.

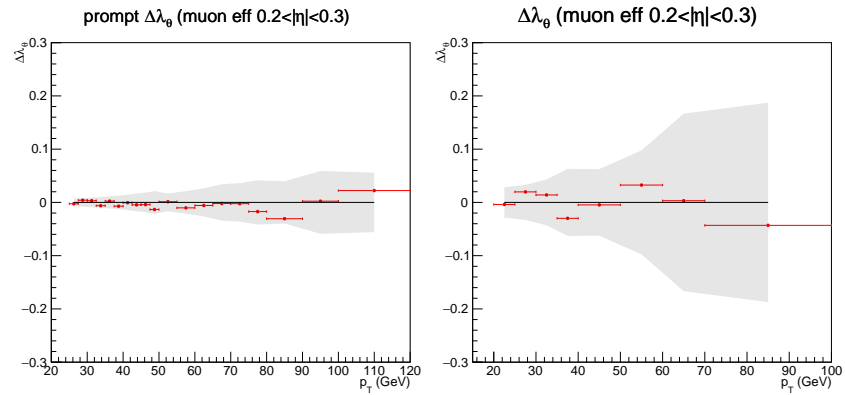


Figure 44: Differences between the  $\lambda_\theta$  values obtained when rejecting events with at least one muon in the  $0.2 < |\eta| < 0.3$  region and the baseline procedure, compared to the statistical uncertainties of the baseline measurement (grey band), for the  $J/\psi$  (left) and  $\psi(2S)$  (right) analyses.

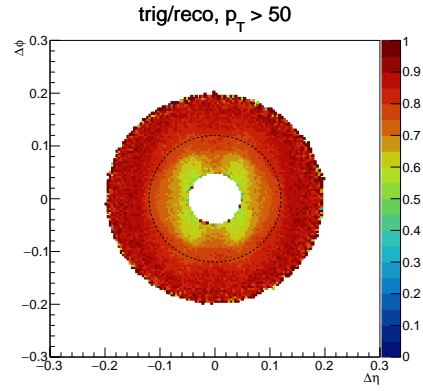


Figure 45: Ratio between simulated 2D event distributions, after over before applying the trigger emulation, for  $J/\psi$  dimuons of  $p_T > 50\text{GeV}$ , in the  $\Delta\phi$  vs.  $\Delta\eta$  plane.

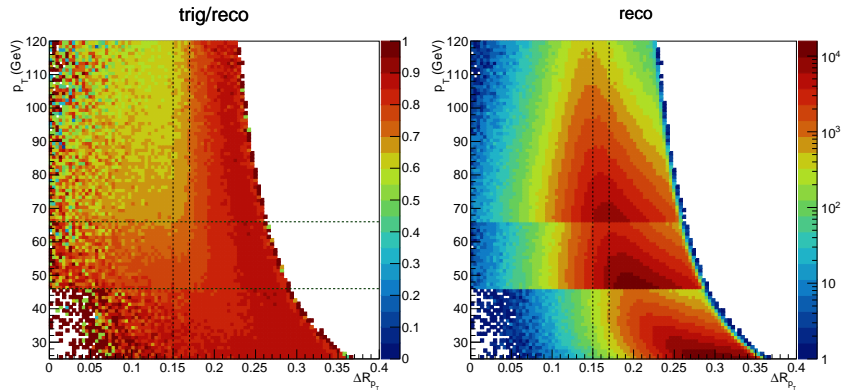


Figure 46: Left: Ratio between simulated 2D event distributions, after over before applying the trigger emulation, for  $J/\psi$  dimuons of  $p_T > 50\text{GeV}$ , in the  $p_T$  vs.  $\Delta R_{p_T}$  plane. Right: Corresponding event distribution before applying the trigger emulation.

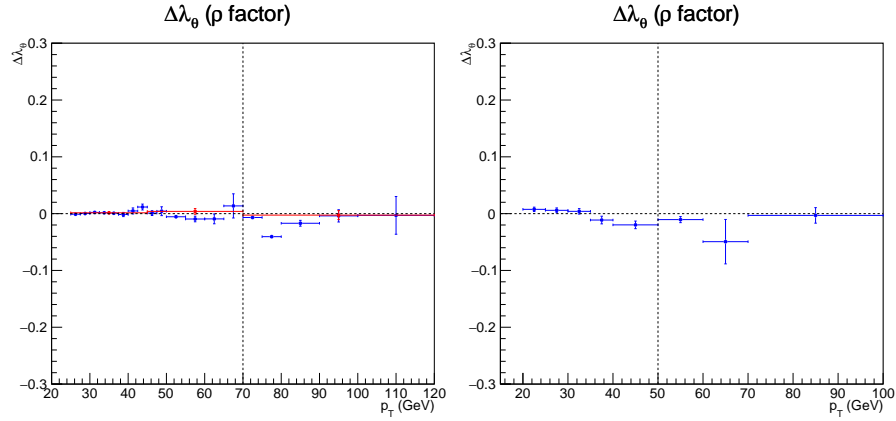


Figure 47: Difference between the  $\lambda_\theta$  values measured with and without applying the  $\Delta R_{p_T}$  cuts, vs.  $p_T$ , for the  $J/\psi$  (left) and  $\psi(2S)$  (right) analyses.

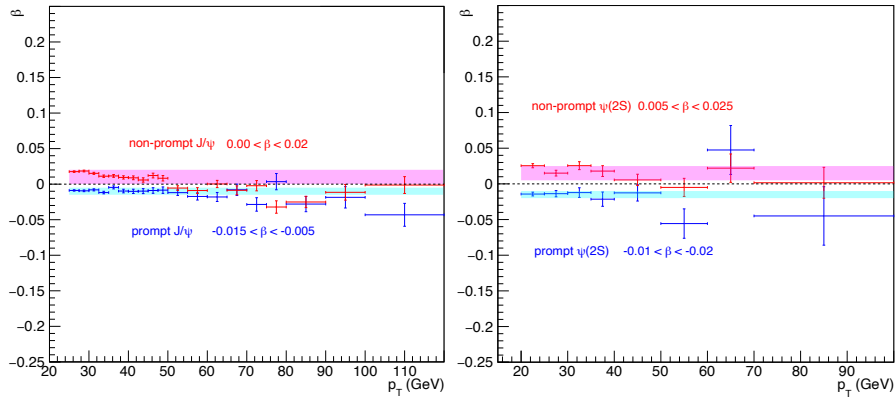


Figure 48: Fitted  $\beta$  values, versus  $p_T$ , for the prompt (blue) and non-prompt (red)  $J/\psi$  (left) and  $\psi(2S)$  (right) analyses. The bands represent our estimates for the  $\beta$  ranges.

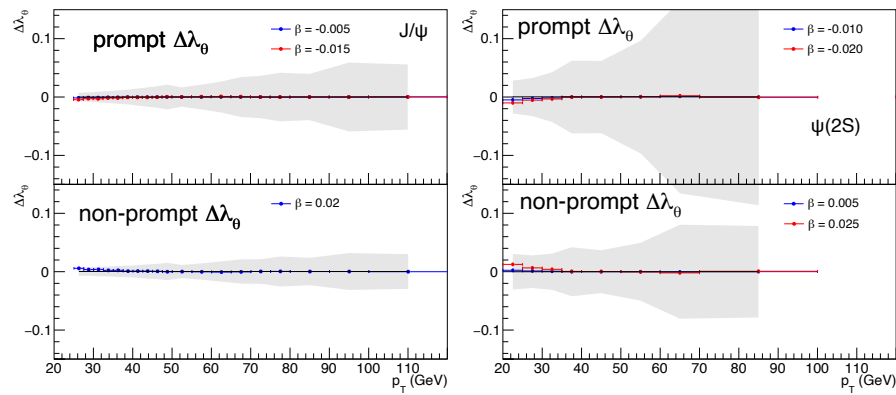


Figure 49: Difference  $\Delta\lambda_\theta$  between the  $\lambda_\theta$  values measured with the reweighted acceptance maps (using the  $\beta$  values mentioned in the legends), and the baseline values, vs.  $p_T$ , for the  $J/\psi$  (left) and  $\psi(2S)$  (right) analyses.

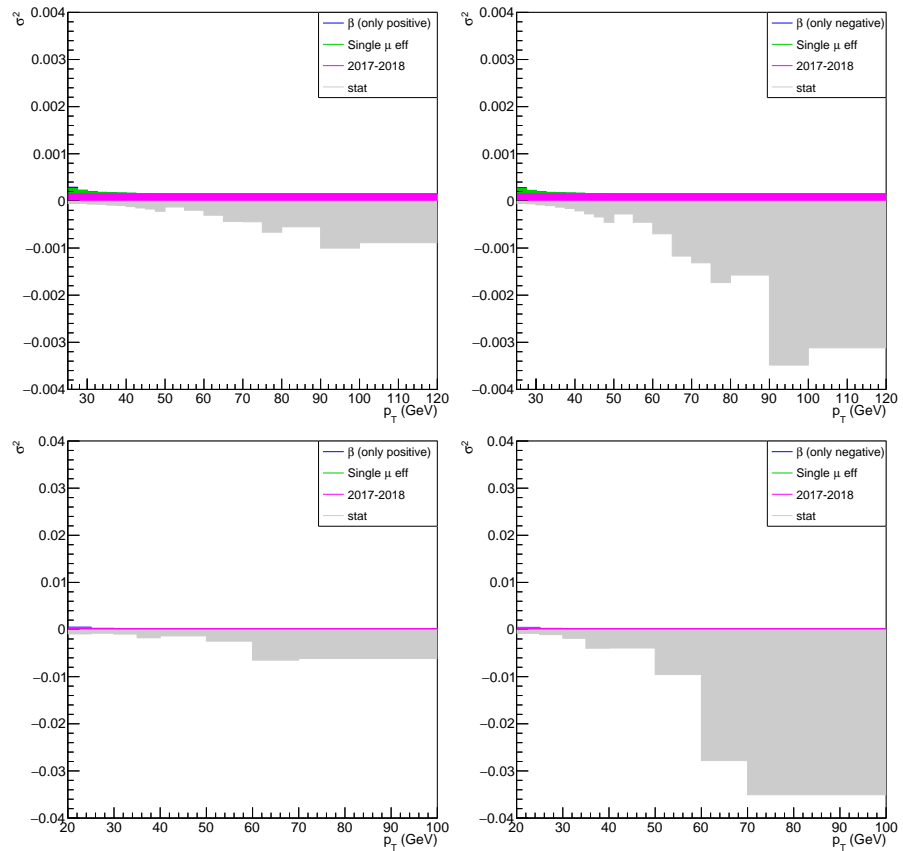


Figure 50: Systematic uncertainties squared and stacked, on the positive hemisphere, and statistical uncertainties squared, on the negative hemisphere, for the non-prompt (left) and prompt (right)  $J/\psi$  (top) and  $\psi(2S)$  (bottom) measurements.

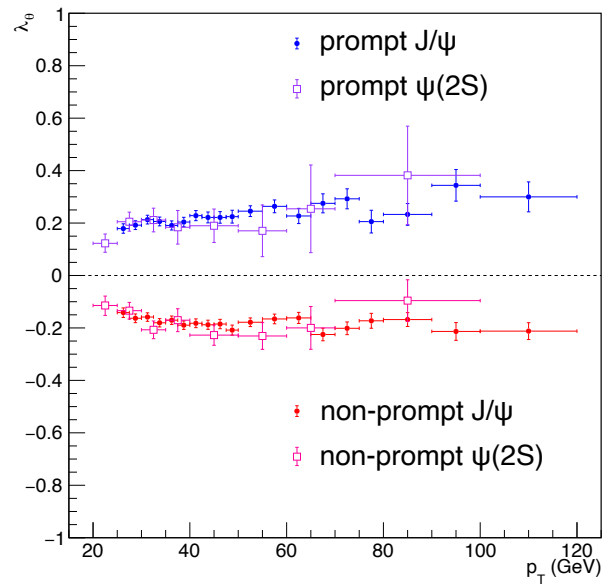


Figure 51:  $\lambda_\theta$  parameter measured, as a function of  $p_T$ , for the prompt and non-prompt  $J/\psi$  and  $\psi(2S)$  mesons, as indicated in the legends. The vertical bars represent the statistical and systematic uncertainties summed in quadrature.

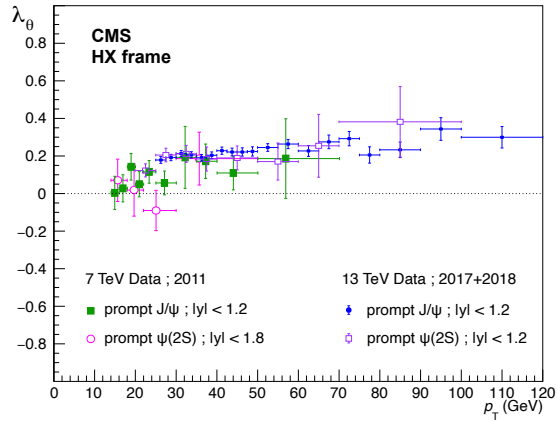


Figure 52:  $\lambda_\theta$  parameter measured, as a function of  $p_T$ , for prompt  $J/\psi$  and  $\psi(2S)$  mesons produced in  $pp$  collisions at  $\sqrt{s} = 13\text{TeV}$  (this analysis) and at  $\sqrt{s} = 7\text{TeV}$  (BPH-13-003 analysis [5]). The vertical bars represent the statistical and systematic uncertainties summed in quadrature.

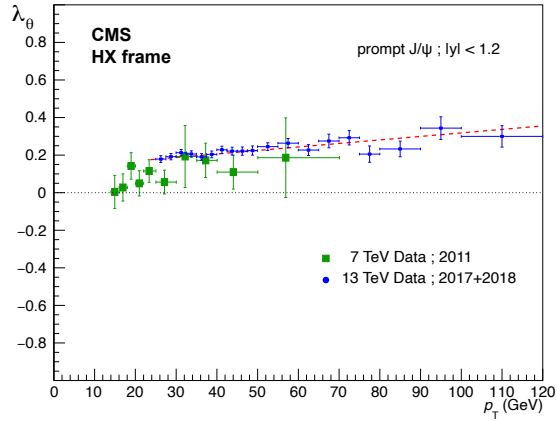


Figure 53: Same as the previous figure but without the  $\psi(2S)$  points, to provide a better picture of the (more precise)  $J/\psi$  measurements.